The Astrophysical Journal, 937:20 (18pp), 2022 September 20 https://doi.org/10.3847/1538-4357/ac86c7

On the Robustness of the Velocity Anisotropy Parameter in Probing the Stellar Kinematics in Milky Way–Like Galaxies: Takeaway from TNG50 Simulation

Razieh Emami[1], Lars Hernquist[1], Mark Vogelsberger[2], Xuejian Shen[3], Joshua S. Speagle (沈佳士)[4,5,6,12], Jorge Moreno[7], Charles Alcock[1], Shy Genel[8,9], John C. Forbes[8], Federico Marinacci[10], and Paul Torrey[11]
[1] Center for Astrophysics | Harvard & Smithsonian, 60 Garden Street, Cambridge, MA 02138, USA; razieh.emami_meibody@cfa.harvard.edu
[2] Department of Physics, Kavli Institute for Astrophysics and Space Research, Massachusetts Institute of Technology, Cambridge, MA 02139, USA
[3] TAPIR, California Institute of Technology, Pasadena, CA 91125, USA
[4] David A. Dunlap Department of Astronomy & Astrophysics, University of Toronto, 50 St. George Street, Toronto, ON M5S 3H4, Canada
[5] Dunlap Institute for Astronomy and Astrophysics, University of Toronto, 50 St. George Street, Toronto, ON M5S 3H4, Canada
[6] Department of Statistical Sciences, University of Toronto, 100 St. George Street, Toronto, ON M5S 3G3, Canada
[7] Department of Physics and Astronomy, Pomona College, Claremont, CA 91711, USA
[8] Center for Computational Astrophysics, Flatiron Institute, New York, USA
[9] Columbia Astrophysics Laboratory, Columbia University, 550 West 120th Street, New York, NY 10027, USA
[10] Department of Physics & Astronomy "Augusto Righi," University of Bologna, via Gobetti 93/2, 40129 Bologna, Italy
[11] Department of Astronomy, University of Florida, 211 Bryant Space Sciences Center, Gainesville, FL 32611, USA
Received 2022 February 17; revised 2022 July 20; accepted 2022 August 2; published 2022 September 19

Abstract

We analyze the velocity anisotropy of stars in real and energy space for a sample of Milky Way–like galaxies in the TNG50 simulation. We employ different selection criteria, including spatial, kinematic, and metallicity cuts, and make three halo classes ($\mathcal{A}$–$\mathcal{C}$) that show mild-to-strong sensitivity to different selections. The above classes cover 48%, 16%, and 36% of the halos, respectively. We analyze the β radial profiles and divide them into either monotonically increasing radial profiles or ones with peaks and troughs. We demonstrate that halos with monotonically increasing β profiles are mostly from class $\mathcal{A}$, while those with peaks/troughs are part of classes $\mathcal{B}$ and $\mathcal{C}$. This means that care must be taken, as the observationally reported peaks/troughs might be a consequence of different selection criteria. We infer the anisotropy parameter β energy space and compare that against the β radial profile. It is seen than 65% of halos with very mild sensitivity to different selections in real space are those for which the β radial and energy profiles are closely related. Consequently, we propose that comparing the β radial and energy profiles might be a novel way to examine the sensitivity to different selection criteria and thus examining the robustness of the anisotropy parameter in tracing stellar kinematics. We compare simulated β radial profiles against various observations and demonstrate that, in most cases, the model diversity is comparable with the error bars from different observations, meaning that the TNG50 models are in good overall agreement with observations.

Unified Astronomy Thesaurus concepts: Galaxy stellar halos (598); Milky Way Galaxy (1054); Hydrodynamical simulations (767)

1. Introduction

Halo stars comprise only ∼1% of the stellar mass in the Milky Way (MW). Nevertheless, they provide remarkable information about the assembly history of our Galaxy. Stars belonging to the stellar halo are typically old and metal-poor, pointing to the halo's ancient origin. By tracking the current orbits of stars, we may get some information on their motions at early times. Consequently, we may use their current orbit to track the kinematics of their progenitors, such as external satellite galaxies or the gas clouds where these stars formed initially (Hattori et al. 2013). Furthermore, stellar kinematics can also be employed for studying the distribution of the gaseous component (Cinzano & van der Marel 1994; Krajnović et al. 2005; Adams et al. 2012, 2014).

A widely used technique to model the galactic mass distribution is the Jeans dynamical modeling (Jeans 1915; Binney 1980; Merritt 1985; Dejonghe & Merritt 1992; Courteau et al. 2014). Motivated by this, it is customary to compute the rms of the radial velocity as $v_{\rm rms} \equiv \sqrt{\langle v_r^2 \rangle}$ (El-Badry et al. 2017) and the velocity anisotropy parameter,

$$\beta \equiv 1 - \left(\frac{\sigma_\theta^2 + \sigma_\phi^2}{2\sigma_r^2} \right). \quad (1)$$

Here σ_i refers to the velocity dispersion along the following directions: $i = (r, \theta, \phi)$, and it is calculated as $\sigma_i \equiv \sqrt{\langle v_i^2 \rangle - \langle v_i \rangle^2}$. The velocity anisotropy parameter, hereafter β, was initially introduced by Binney (1980) to measure the orbital structure of a given system. In this parameterization, β ranges from $-\infty$ (for purely tangential orbits) through zero (for completely isotropic motions) to 1 (for purely radial orbits). Radial orbits correspond to $\beta > 0$, while tangential ones have $\beta < 0$. The velocity anisotropy is vital in accurately measuring the mass distribution in dispersion-supported systems, from dwarf spheroidal galaxies (Gilmore et al. 2007; Strigari et al. 2007; Wolf et al. 2010) to massive ellipticals (Dekel et al. 2005).

[12] Banting & Dunlap Fellow.

Direct measurements of β have been somewhat challenging because they require a full 3D map of stellar velocities, which had not been possible until very recently, thanks to the development of the Hubble Space Telescope (HST) and the Gaia mission. Observers commonly measure the line-of-sight (LOS) velocity and use this to infer the β (see, for example, Sirko et al. 2004; Deason et al. 2012; Kafle et al. 2012; King et al. 2015, and references therein). The main reason for this is that, owing to our position in the MW, LOS velocities provide useful information about tangential velocities. However, Hattori et al. (2017) pointed out that since stellar orbits become progressively more radial at larger galactocentric distances, using only LOS velocities may underestimate the β. Consequently, the velocity anisotropy parameter has instead only been measured indirectly via dynamical modeling (see, for example, Cinzano & van der Marel 1994; Diakogiannis et al. 2014a, 2014b, and references therein).

Fortunately, it is now possible to measure tangential velocities for a small sample of stars away from the galactic center by using full 3D velocity measurements (e.g., Smith et al. 2009; Bond et al. 2010; Sohn et al. 2012; Cunningham et al. 2016;; Gaia Collaboration et al. 2018; Watkins et al. 2019, and references therein), although getting a very accurate LOS velocity may require obtaining the spectra.

In observational studies, authors have adopted different assumptions for the $\beta(r)$ profile. For example, it is commonly assumed that either $\beta(r)=$ Const (e.g., Łokas et al. 2005; Koch et al. 2007; Walker et al. 2007; Battaglia et al. 2008; Łokas 2009; Walker et al. 2009, and references therein), or $\beta(r)$ varies radially (e.g., Kleyna et al. 2001; Wilkinson et al. 2004; Mamon & Łokas 2005; Gilmore et al. 2007; Battaglia et al. 2008; Mamon et al. 2013; Mashchenko 2015). While a constant β is well suited to measure the mass of the MW, a radially varying β may have additional power in probing the MW's accretion history (e.g., Cunningham et al. 2019; Loebman et al. 2018; Bird et al. 2021). Morrison et al. (1990) used the G and K giants (located up to a few kiloparsecs from the Sun) and estimated $\beta \approx 0.5$. Chiba & Yoshii (1998) estimated $\beta = 0.52 \pm 0.07$ from a sample of metal-poor halo stars near the Sun. Beyond the solar neighborhood, one may also estimate β with LOS velocities by adopting mass-distribution models of the galaxy. Appropriate tracers include blue horizontal branch (BHB) stars, K giants, and F-type stars (see, e.g., Sommer-Larsen et al. 1994; Thom et al. 2005; Kafle et al. 2012; King et al. 2015, and references therein). Smith et al. (2009) used halo subdwarfs from the Sloan Digital Sky Survey (SDSS) and estimated $\beta = 0.69 \pm 0.01$. Bird et al. (2019) used K giants from the Large Sky Area Multi-Object Fiber Spectroscopic Telescope (LAMOST) catalog and measured β as a function of galactocentric radius.

On the theory front, simulations of MW-like galaxies often result in radially increasing β profiles (e.g., Diemand et al. 2005; Abadi et al. 2006; Sales et al. 2007; Rashkov et al. 2013; Kafle et al. 2012; Stinson et al. 2013). As shown by Loebman et al. (2018), analyses of this kind unveil more complex structures in β and the halo in general (e.g., Beers et al. 2012; Schuster et al. 2012; Zuo et al. 2017).

In this paper, we analyze the stellar kinematics inferred from the stellar velocity anisotropy parameter, β, in a sample of MW-like galaxies from the TNG50 run of the Illustris-The-Next-Generation (IllustrisTNG) project. The enhanced resolution in TNG50 makes it possible to analyze radial β profiles very accurately, near the level of the zoom-in simulations, and also consider the impact of cosmic evolution and mergers of a larger statistical population, as the TNG50 simulation has many more galaxies in the box. We analyze the β radial and energy profiles at redshift $z = 0$ and investigate their dependencies on various selection criteria, including spatial and kinematic cuts, as well as the ones coming from some metallicity cuts.

We design a halo classification based on the sensitivity levels of the β profile to various selection criteria and place halos in three classes. The $\mathcal{A}$ class refers to halos with a very mild sensitivity to different selections. Halos that are part of class $\mathcal{B}$ show some level of sensitivity to different selections, and those associated with $\mathcal{C}$ show a very strong dependency on model selections. We show that 48%, 16%, and 36% of the halos are part of classes $\mathcal{A}$–$\mathcal{C}$, respectively. We analyze the β radial profile and show that it can be divided into monotonically increasing profiles or the ones with peaks/troughs, which contain 32% and 68% of the halos, respectively. It is shown that the β profile from the monotonically increasing class smoothly increases from the interior to the exterior part of the halo, while the β from the class with peaks/troughs experiences some local fluctuations. We further demonstrate that almost all of the halos from the first class are part of category $\mathcal{A}$, with only one exception. On the contrary, members of the class with peaks/troughs are mostly part of categories $\mathcal{B}$ and $\mathcal{C}$, with only 29% of them being part of category $\mathcal{A}$. This means that care should be taken in interpreting the observed peaks/troughs, as they might depend on the actual selection criteria.

We infer the impact of different metallicity and eccentricity cuts in the β radial profile and also investigate the impact of different stellar orbital types, such as the radial, prograde, and retrograde on the β radial profile.

Moving in the energy space, we infer and compare the β radial and energy profiles against each other and make another halo classification based on their differences. It is seen that 65% of the halos with very mild sensitivity on different selection criteria in the real space are among those for which the β radial and energy profiles are closely related. On the contrary, halos in which the β radial and energy profiles are rather different are entirely coming from category $\mathcal{C}$. This again establishes that one should be careful when drawing any conclusions from these classes. Furthermore, we propose that one quantitative way to check if the observational results are very robust is to also compute the β energy profile and compare that with the β radial profile. Based on our conclusion, it is likely that those with very similar profiles are also very robust against altering the selection criteria.

It must be emphasized that our current β analysis in the real and energy spaces and their correlations is purely theoretical and based on a full awareness of the gravitational potential for the MW. From the observational perspective, we may only estimate the potential to some extent. Furthermore, the current paper is not aimed at proving that we identify an unbiased sample of stars using this comparison, but rather that for a given sample of stars, such a comparison between the β radial and energy profiles likely indicates how the sample may show sensitivities to changing different selection criteria.

Motivated by the aforementioned halo classification, throughout this paper, we make a subhalo sample of four galaxies from each of the above classes and study their

Table 1
Linking between the Subhalo ID with the Galaxy Number in Our Sample of MW-Like Galaxies in TNG50

1 ↦ 476266	2 ↦ 478216	3 ↦ 479938	4 ↦ 480802	5 ↦ 485056
6 ↦ 488530	7 ↦ 494709	8 ↦ 497557	9 ↦ 501208	10 ↦ 501725
11 ↦ 502995	12 ↦ 503437	13 ↦ 505586	14 ↦ 506720	15 ↦ 509091
16 ↦ 510585	17 ↦ 511303	18 ↦ 513845	19 ↦ 519311	20 ↦ 522983
21 ↦ 523889	22 ↦ 529365	23 ↦ 530330	24 ↦ 535410	25 ↦ 538905

behavior thoroughly. This includes halos [4, 12, 20, 25], which are members of categories [$\mathcal{A}$, $\mathcal{B}$, $\mathcal{B}$, $\mathcal{C}$], respectively.

Ultimately, we overlay our theoretical outcomes, with a few different selection criteria, on top of the most recent observational results and compare them with each other. Our comparison is made both at the level of isolated data points as well as the extended observations in which the β profile is reported in more than a single point. We made a comparison between the TNG simulations and the most recent observational data, where we see that for each halo, there are some data points that easily pass through the profile.

This paper is organized as follows. Section 2 summarizes the TNG50 simulation and our sample of MW-like galaxies. Section 3 links stellar metallicity to other stellar properties. Section 4 computes the radial and energy velocity anisotropy profiles. Section 5 compares our simulated radial-β profiles against the observations. Lastly, Section 6 presents our conclusions.

2. TNG50 Simulation

The TNG50 is the highest-resolution run of the suite of large-scale series of IllustrisTNG simulations (e.g., Pillepich et al. 2019; Nelson et al. 2019a). It provides an excellent combination of the volume and resolution close to the level of zoom-in simulations (e.g., Monachesi et al. 2016; Grand et al. 2018; Hani et al. 2019) and thus provides a natural avenue to investigate the impact of galaxy evolution with very high resolution. It evolves the evolution of supermassive black holes (SMBHs), dark matter, gas, stars, and magnetic fields within a periodic boundary volume of 51.7 kpc^3. Its softening length is 0.39 comoving kpc h^{-1} for $z \geqslant 1$, reducing to 0.195 proper kpc h^{-1} for $z < 1$.

In TNG50, the model for galaxy formation includes a stochastic, given gas density threshold for the star formation, the evolution of mono-age stellar populations that are being represented by the star particles, the chemical enrichment of the interstellar medium, and the tracking of nine different chemical elements (H, He, C, N, O, Ne, Mg, Si, and Fe), in addition to total gas metallicity and europium. It also includes the gas cooling and heating; the feedback from supernovae, which is in the form of galactic winds; the seeding and growth of SMBHs; and the injection of the energy and momentum from SMBHs into the surrounding gas.

Using various selection criteria, such as dark matter halo mass, and choosing the rotationally supported stellar population in Emami et al. (2021a, 2021b, 2021c), we created a sample of 25 MW-like galaxies in the TNG50 simulation. In Table 1, we present the ID number of the chosen galaxies in our sample. This paper probes the structure of the stellar distribution, ignoring the impact of satellites, with stellar kinematics as the tracer. We also analyze different stellar properties, including stellar age, metallicity, and the stellar velocity anisotropy profile. One of our goals is to investigate how different selection criteria based on these quantities impact radial velocity anisotropy profiles.

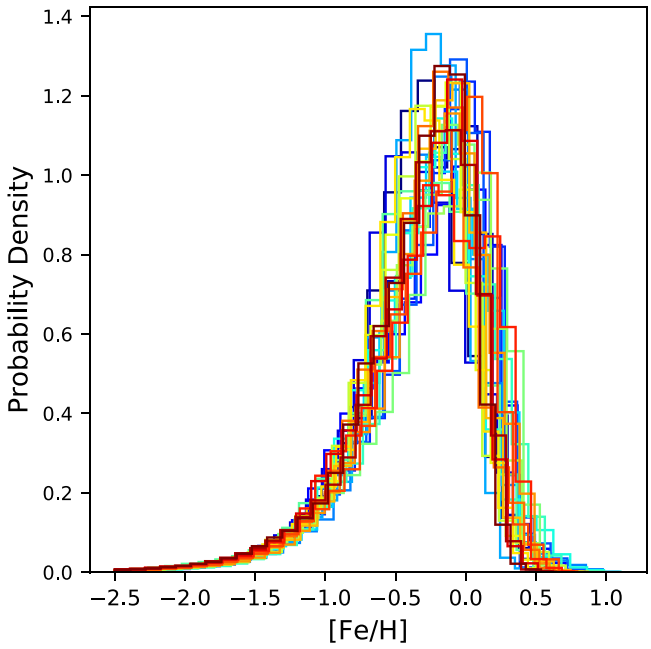

Figure 1. Probability density distribution of stellar metallicity in our MW-like galaxy sample. It is evident that stars from different galaxies have quite similar metallicity distributions. Different colors refer to various galaxies. Low metallicities are in the tail of the distribution.

3. Stellar Metallicity

Since the metallicity cut is one of the key ingredients in our stellar sample selection, in what follows, we study the correlation between stellar metallicity and various other stellar properties, including the stellar age, the spatial metallicity distribution, and the stellar velocity.

First, we present the stellar metallicity distribution. Figure 1 presents the 1D probability density distribution of all of the stars in different galaxies in our sample. Quite interestingly, stars from different galaxies in our sample seem to have very similar metal distribution. Moreover, it is evident that stars with low metallicity are in the tail of the distribution, while those with [Fe/H] in the range [−0.5–0.0] sit on the peak of the distribution. It is intriguing to see how different metallicity-based cuts might affect the velocity anisotropy of stars. In Section 4.2, we get back to this question in depth.

3.1. Stellar Age versus Metallicity

Next, we study the correlation between the stellar age and the stellar metallicity. Figure 2 presents [Fe/H] versus stellar

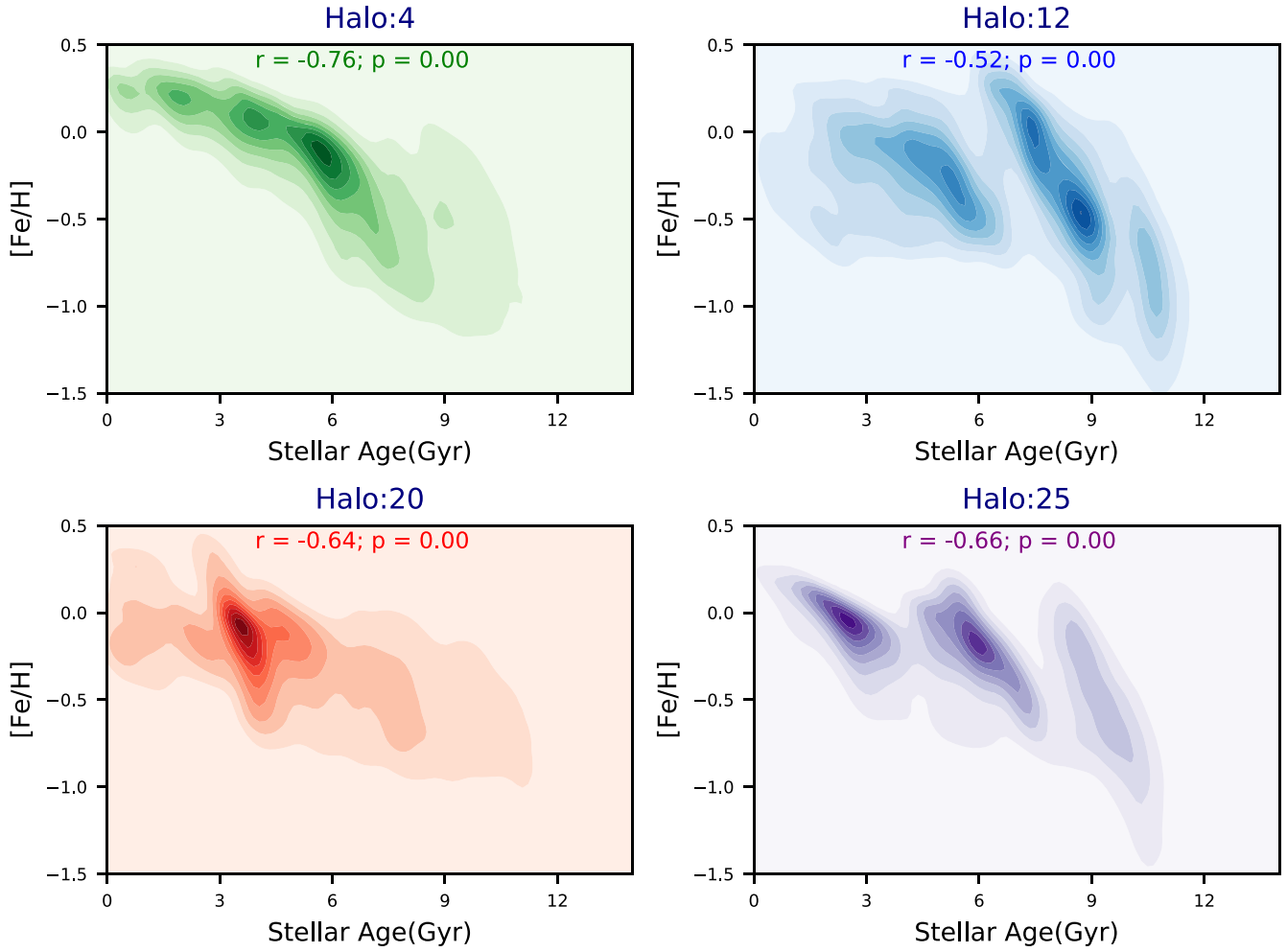

Figure 2. The 2D correlation of stellar age vs. metallicity for a subsample of four galaxies from our MW-like galaxy sample. The Spearman correlation is negative, indicating that metal-poor stars are older than metal-rich ones.

age for a subsample of four galaxies from our sample, including galaxies [4, 12, 20, 25]. As already stated above, these halos are members of distinct categories. In each case, we have inferred the Spearman correlation, hereafter r, between the stellar metallicity and the age.

From the plot, it is inferred that while in some cases, such as galaxy 4, the stellar metallicity is smoothly declining with increasing stellar age, others, such as galaxy 12, show a break and thus a discrete profile of age versus [Fe/H] indicating that their associated stars might have different origins. For instance, they might be accreted as a satellite merged onto the galaxy or have arisen from star-forming gas out of a galaxy merger, etc. Intriguingly, such a break reduces the Spearman correlation, as we end up having a bimodal age–[Fe/H] relation.

Furthermore, it is seen that in some cases, such as galaxy 20, there is a peak of star formation at an intermediate time, around 4.5 Gyr, that might be an indication of a major merger in the history of the galaxy. Comparing the Spearman correlation of galaxies 4 and 20, we may argue that such a local peak may have slightly diminished the r in galaxy 20. This is better seen when we compare these with galaxy 25, in which we have few distinct bursts of stars, and its $|r|$ is slightly higher than galaxy 20, while it is still less than the 1 for galaxy 4.

In summary, our analysis demonstrate that in all cases, $|r| \geqslant 0.5$, showing a moderate-to-large negative correlation between the stellar age versus metallicity depending on galaxy ancient history. Owing to the above correlation between the stellar age versus metallicity, different metallicity cuts naturally pick stars with different ages and allow us to indirectly probe the velocity distribution of young versus old stars. In Section 4.2, we address this question.

3.2. Spatial Distribution of Metallicity

Below, we explore the possible correlation between the location of stars and the stellar metallicity. Figure 3 presents the 2D distribution of the stellar radii versus the stellar metallicity for a subsample of four members of our galaxy sample. From the plot, it is inferred that metal-rich stars are generally closer to the galaxy center than metal-poor ones, in line with the observations (e.g., Huang et al. 2015; Anders et al. 2017; Dietz et al. 2020; Santucci et al. 2020). Combining that with the above age–metallicity relation, we argue that galaxies in our sample mostly have inside-out star formation, in agreement with the recent studies of the inside-out growth of the stellar disk (see, e.g., Frankel et al. 2019; Bird et al. 2021; Johnson et al. 2021, and references therein). The slope of the metallicity gradient varies from galaxy to galaxy. Some galaxies show a more extended metallicity gradient, while others have a more concentrated profile. Furthermore, the extent to which we infer the dominant population of stars is also correlated with their

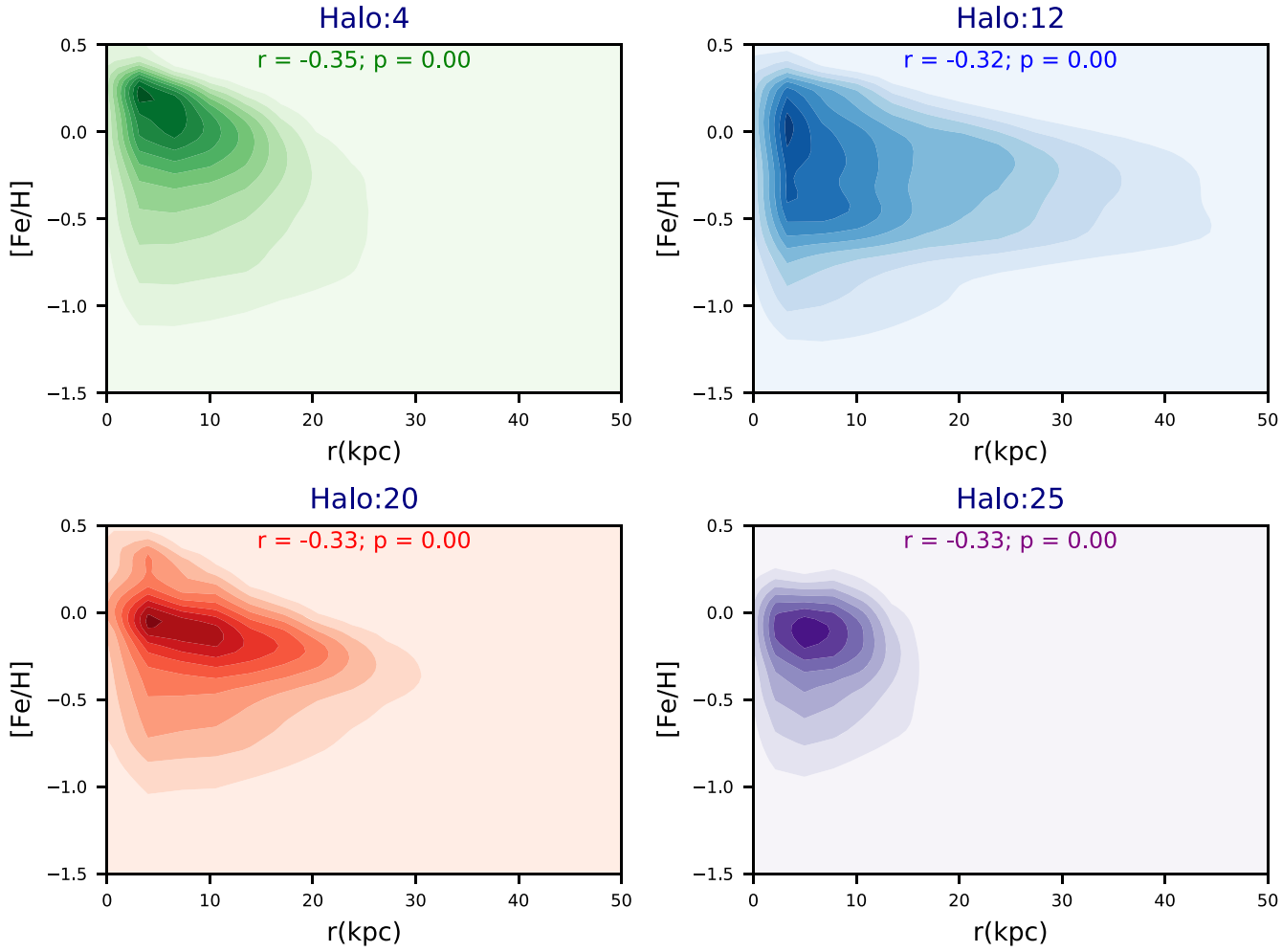

Figure 3. The 2D correlation of the stellar distance vs. stellar metallicity for a subsample of four galaxies from our MW-like galaxy sample. The Spearman correlation is modest and negative, indicating that metal-rich stars are located closer to the galactic center.

age–metallicity profile. For instance, galaxy 12 shows a more extended profile, in line with our former argument of being affected by mergers. This makes sense, as galaxy mergers are expected to expand and dislocate stars from their original place. Finally, the Spearman correlation between the stellar location and the stellar metallicity is relatively low, indicating that there are some other factors in locating the stars than their metallicity.

3.3. Metallicity versus Velocity

As a final step, here we study the correlation between the stellar speed and the stellar metallicity. Figure 4 presents the 2D distribution of the stellar velocity amplitude versus the stellar metallicity for a subsample of four galaxies from our MW-like galaxy sample. In each case, we infer the Spearman correlation between these quantities, demonstrating that they are uncorrelated. This makes sense, as our galaxy sample obeys the well-known Tully–Fisher relation (Tully & Fisher 1977), as well as the mass–metallicity relation (Gallazzi et al. 2005; Kewley & Ellison 2008). The velocity peaks stand between 200 and 300 km s^{-1}, indicating that the kinematic of stars inferred in this sample of MW-like galaxies are consistent with the rotational velocity of stars seen in the MW disk.

4. Velocity Anisotropy: β

In this section, we analyze the radial profile of the velocity anisotropy as defined in Equation (1). In our calculations, we use various selection criteria. Recall that the β parameter characterizes various stellar orbital types. We present the 2D distribution map for the stellar location out of different selection criteria. Furthermore, we study the impact of changing the metallicity cuts, eccentricity, and different orbital types on the β radial profile, $\beta(r)$. Finally, we analyze the β energy profile and compare that with the β radial profile.

4.1. The β Radial Profile

To infer the $\beta(r)$ for each galaxy, we adopt a coordinate system where the z-axis (oriented along with the total angular momentum of stars) is orthogonal to the disk, with (x–y) being chosen randomly (right-handed and orthogonal to each other) on the disk plane. As a next step, since $\beta(r)$ deals with radial and tangential vectors, we make a transformation to the spherical coordinate system (for both the coordinate and the velocity vectors). We adopt 15 linearly distributed radial bins between 1 and 100 kpc, and, for each of them, we compute the radial and tangential velocity dispersions. We force each bin to contain at least 100 stellar particles (in practice, many of them have over 1000 stellar particles). We choose different selection

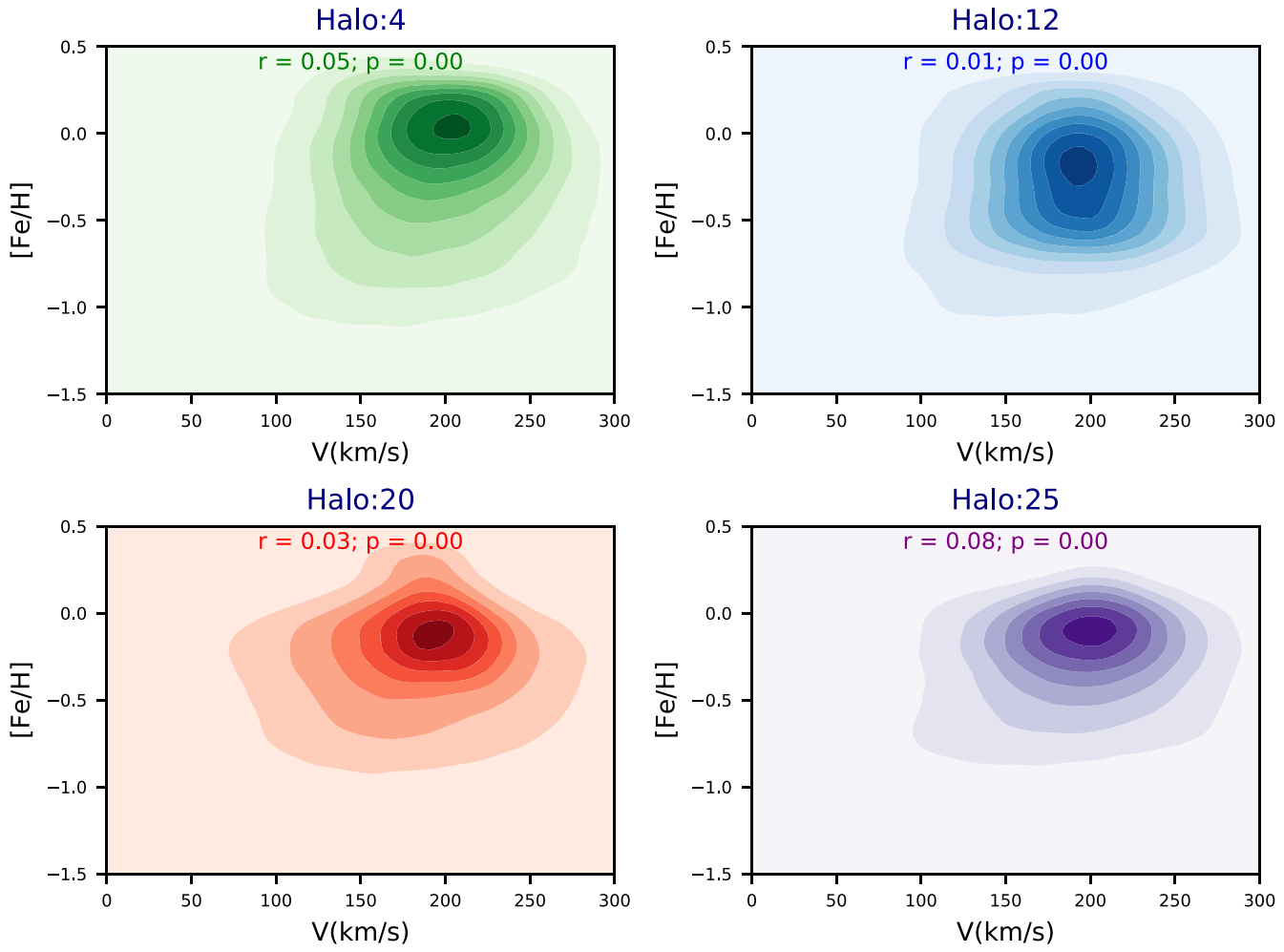

Figure 4. The 2D correlation of the stellar velocity amplitude vs. the stellar metallicity for a subsample of four galaxies from our MW-like galaxy sample. It is inferred that the stellar velocity is largely uncorrelated with the stellar metallicity, as stellar speed is mainly concentrated between 200 and 300 km s^{-1}, in agreement with the observed rotational velocity of stars in our MW.

criteria for stars. Figure 5 presents the β radial profile for four different cases as listed below.

1. The dashed black line refers to the kinematically chosen stars with $\epsilon < 0.7$, where ϵ is defined by Equation (3) in Emami et al. (2021b). Theoretically, this means that we are choosing halo stars (see, e.g., Monachesi et al. 2019, and references therein). We emphasize that the above threshold is not unique. Nevertheless, it is robust to small variations.
2. The blue dotted–dashed line describes a hybrid selection of $[\mathrm{Fe/H}] < -1.3$ with $|Z| \geqslant 5$ kpc. This choice is based on the LAMOST data (Bird et al. 2019).
3. With the solid red lines, we relax the metallicity cut and only choose stars above the disk plane $|Z| \geqslant 5$ kpc.
4. The dotted yellow line refers to the case with no spatial cut. At first glance, it seems that in some cases, the velocity anisotropy of stars with completely different selection criteria might be somewhat close.

Before we analyze the β radial profile above in depth, here we present a spatial map of stars inferred from different selection cuts. This enables us to develop an intuition on the impact of different selection criteria on the spatial distribution of stars. Figure 6 presents an image for a typical galaxy, galaxy 1, along with three different projections. Top to bottom, the rows present the 2D surface density map of stars with $\tilde{r} \geqslant 1$, $\tilde{r} \geqslant 1$, $\epsilon \leqslant 0.7$, $\tilde{r} \geqslant 1$, $\tilde{Z} \geqslant 5$, and $\tilde{r} \geqslant 1$, $\tilde{Z} \geqslant 5$, $[\mathrm{Fe/H}] \leqslant -1.3$. Here $\tilde{X} \equiv X/$ kpc with $X = (r, Z)$. Interestingly, the kinematic cut of $\epsilon \leqslant 0.7$ and the spatial cut of $\tilde{Z} \geqslant 5$ both decrease the spiral structure of the galaxy in the disk plane. While, the current metallicity cut diminishes the population of stars substantially, as $[\mathrm{Fe/H}] \leqslant -1.3$ sits on the tail of the stellar distribution.

Having fully described the details of different lines as presented in Figure 5, below, we analyze the β radial profile inferred from each of them in depth and make a halo classification based on the behavior of the β radial profile.

4.1.1. β Inferred Halo Classification from Selection Criteria

Having presented the β radial profile for halos in our sample, here we make a halo classification based on the sensitivity of the β radial profiles to different selection criteria. The goal is to quantify the sensitivity of β to different stellar orbital types achieved from different selections.

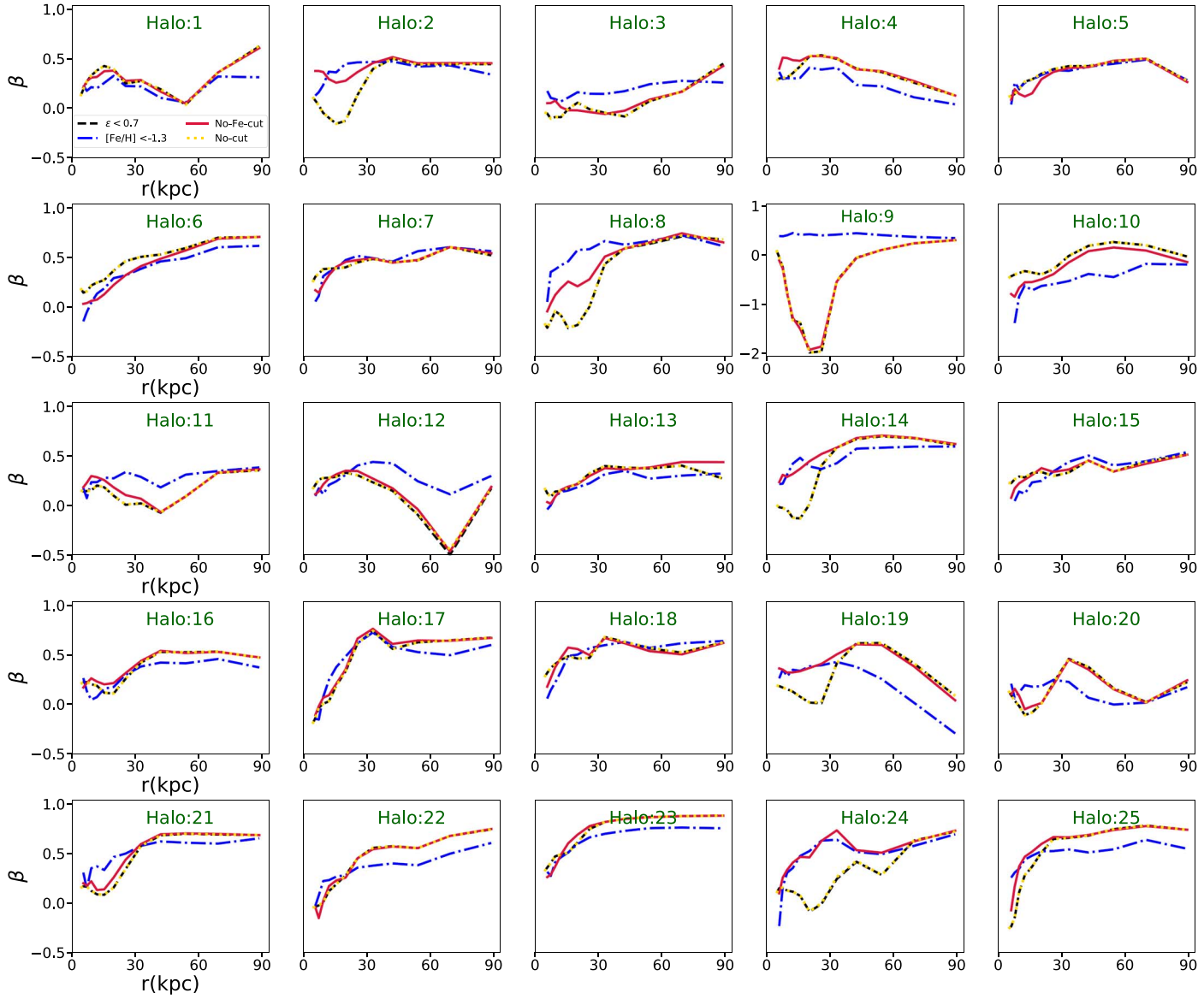

Figure 5. The β radial profile for stars inferred using different selection criteria. Dashed black, blue dotted–dashed, solid red, and dotted yellow lines present β inferred from stars with kinematic, metallicity-based, spatial cut, and no cut as was used in computing the β, respectively.

In our analysis, for every galaxy, we use the following empirical classifier:

$$\delta\beta \equiv \frac{\sum_i |\beta_i^{\rm Fe} - \beta_i^{\rm No-cut}|}{\sum_i |\beta_i^{\rm No-cut}|}, \tag{2}$$

where $\beta_i \equiv \beta(r_i)$ is used for the sake of brevity. In addition, in Equation (2), $\beta_i^{\rm Fe}$ refers to the hybrid selection of $[{\rm Fe/H}] < -1.3$ with $|Z| \geqslant 5$ kpc, while $\beta_i^{\rm No-cut}$ stands for the case with no spatial cut, as described above. The selection of $\beta_i^{\rm Fe}$ and $\beta_i^{\rm No-cut}$ in the halo classifier is due to the visual differences seen in the curves associated with them, as presented in Figure 5. As a next step, we define distinct halo classes based on the magnitude of $\delta\beta$ as listed below.

1. *Category* $\mathcal{A}$: $\delta\beta \leqslant 0.35$. Halos that are part of this category show the least sensitivity to different selection criteria. There are 12 halos in this category, including halos [1, 4, 5, 6, 7, 13, 15, 16, 17, 18, 22, 23]. This shows that β is a very robust quantity in about 48% of the halos in our sample.
2. *Category* $\mathcal{B}$: $0.35 \leqslant \delta\beta \leqslant 0.70$. Halos in this class show a mild response to different selection criteria. There are four halos in this class, including halos [10, 12, 21, 25].
3. *Category* $\mathcal{C}$: $\delta\beta \geqslant 0.70$. Halos belonging to this class show a strong dependency on different selections in β calculation. There are nine halos in this class, including halos [2, 3, 8, 9, 11, 14, 19, 20, 24]. This demonstrates that in 36% of the halos in our sample, β is not a robust quantity, as it depends on different selection criteria.

Figure 7 presents the radial profile of the fractional difference between $\beta_i^{\rm Fe}$ and $\beta_i^{\rm No-cut}$ for halos from different classes. In each case, we present

$$\Delta\beta(r) \equiv \left(\frac{\beta^{\rm Fe}(r)}{\beta^{\rm No-cut}(r)}\right) - 1, \tag{3}$$

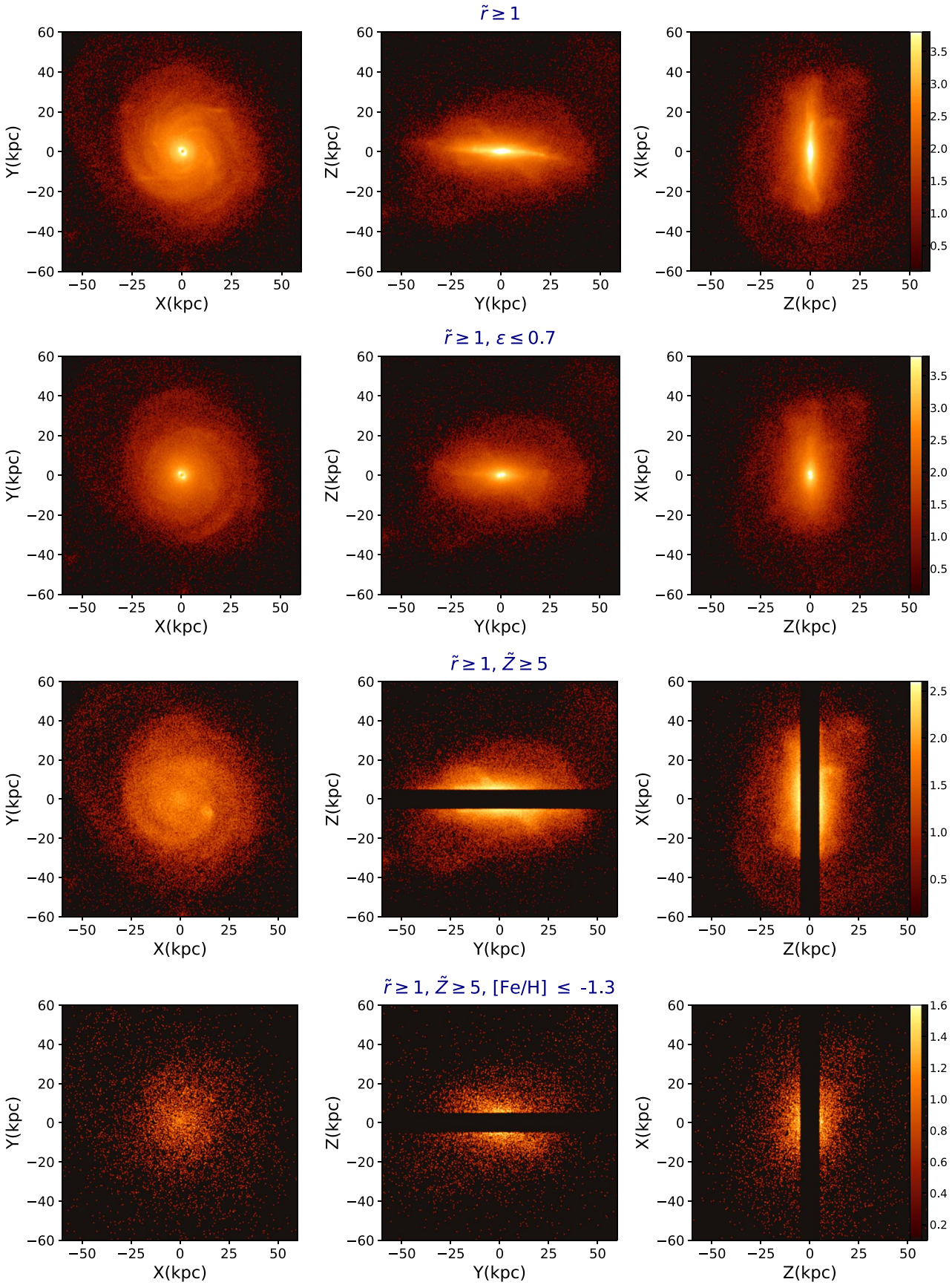

Figure 6. Face-on (left) and (two) edge-on (middle-right) projections of stars in galaxy 1 in our sample. Down rows present the spatial distribution of stars from $\tilde{r} \geqslant 1$, $\tilde{r} \geqslant 1$, $\epsilon \leqslant 0.7$, $\tilde{r} \geqslant 1$, $\tilde{Z} \geqslant 5$ and $\tilde{r} \geqslant 1$, $\tilde{Z} \geqslant 5$, [Fe/H] $\leqslant -1.3$. The color bars refer to the surface number density of stars in different projections.

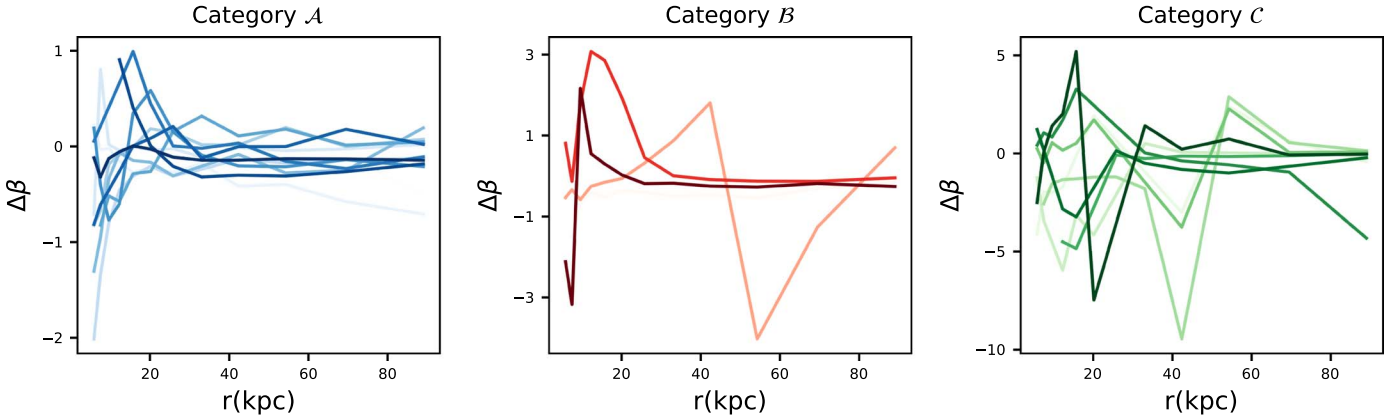

Figure 7. Radial profile of $\Delta\beta(r) \equiv (\beta^{\rm Fe}/\beta^{\rm No-cut})(r) - 1$ for halos from different categories. As stated in Section 4.1.1, halos from categories $\mathcal{A}$–$\mathcal{C}$ show little to very strong response on different selection criteria for β. In addition, it is inferred that, on average, halos from category $\mathcal{A}$ show smoother radial profiles than the other two classes. This is clarified in Figure 8.

eliminating the points for which the denominator gets below 0.05. From the figure, it is inferred that halos belonging to category $\mathcal{A}$ show, on average, smoother radial profiles than those from category $\mathcal{C}$. Below, we make this point more clear.

4.1.2. Detailed Radial Profile of β

Having identified various halo classes, in what follows, we study the β radial profile in some depth and make a connection to the aforementioned halo categories. Considering different profiles, we are dealing with the following behaviors.

1. *Monotonically increasing.* From Figure 5, it is inferred that in 32% of the halos in our sample, β increases with the radius, implying that farther out from the center, the orbits become progressively more radial (i.e., less tangential) and thus less rotationally dominated. This is in agreement with, e.g., El-Badry et al. (2017). In such cases, the $\beta(r)$ profiles are monotonically increasing (i.e., galaxies 6, 7, 13, 15, 18, 22, 23, and 25). There are no visible peaks or troughs in the β radial profile. Such galaxies are also not sensitive to our various selection criteria (the various lines overlap). So a β radial profile is less biased at identifying distinct stellar orbital types. Comparing the halos from this class with the above halo categories, it is evident that almost all of the halos in this case are from category $\mathcal{A}$. The only exception to this is halo 25, which is part of class $\mathcal{B}$.
2. *Profile with peaks/troughs.* On the contrary, in 68% of cases (e.g., galaxies 1, 2, 3, 4, 5, 8, 9, 10, 11, 12, 14, 16, 17, 19, 20, 21, and 24), $\beta(r)$ experiences visible peaks and troughs, in line with recent observations (e.g., Kafle et al. 2012; Cunningham et al. 2019). About 29% of the halos in this class belong to category $\mathcal{A}$, while the rest are from classes $\mathcal{B}$ and $\mathcal{C}$. As the vast majority of halos with peaks/troughs show mild/strong responses to different selection criteria, care is warranted because the presence or absence of such peaks and troughs might actually depend on different selection criteria. For instance, selecting stars with [Fe/H] < -1.3 typically results in $\beta(r)$ profiles without these features. Figure 8 compares the details of the β profiles in each of the aforementioned cases. In the left panel, we show the β radial profile for monotonically increasing cases, while in the right panel, we present the cases with peaks/troughs.

4.2. Impact of Different Metallicity Cuts on the β Radial Profile

Having presented the β radial profile with the LAMOST-based metallicity cut, here we generalize such selection criteria and study the impact of changing different metallicity cuts on the β radial profile. As already stated in Section 3.1, since the stellar metallicity is negatively correlated with the stellar age, various metallicity cuts somewhat choose stars with different ages. It is then very intriguing to study the impact of the stellar age on the velocity anisotropy.

Figure 9 presents the β radial profile for stars with different spatial cuts versus various metallicity criteria. The top panels present the β profile for stars located at $r \geqslant 1$ kpc, while the bottom panels show the β profile for stars located at $r \geqslant 1$ kpc and $Z \geqslant 5$ kpc. In each row, from left to right, we expand over the metallicity cut, from [Fe/H] $\leqslant -1.3$ to $-1.3 \leqslant$ [Fe/H] $\leqslant 0$ to [Fe/H] $\leqslant 0.0$. In line with the conclusion of Section 3.1, we might expect that chosen stars in the left panels are, on average, older than those in the middle panels, while stars in the right panels are a mixture of young and old stars. It is inferred that the left panels have higher βs than the middle panels. This makes sense, as old stars are less rotationally supported, implying lower σ_θ and σ_ϕ and thus higher β. On the contrary, young stars have higher tangential velocity components that correspond to lower values of β. Finally, mixed stars, in the right panels, have βs in between the young and old populations. Interestingly, such a conclusion is almost independent of the spatial cut, as the top and bottom rows are generally quite similar.

4.3. Impact of Different Orbital Types on the β Radial Profile

Next, we explore the impact of stellar orbital types on the β radial profile. Figure 10 shows $\beta(r)$ profiles for the retrograde, radial, and prograde orbits (plus the entire stellar set in the left panel). In each case, we compute $L_z^i \equiv \vec{L}^i \cdot \hat{\vec{L}}_{\rm tot}$ for the ith star, where $\vec{L}^i$ refers to the angular momentum of the ith star, while $\hat{\vec{L}}_{\rm tot}$ describes the unit vector along with the total angular momentum of the stars. We define our three stellar orbital types as follows (Naidu et al. 2020).

a. Retrograde orbits: $L_z^i \leqslant -500$ kpc $\times$ km s^{-1}.
b. Radial orbits: $-500 \leqslant L_z^i/($kpc $\times$ km s$^{-1}) \leqslant 500$.
c. Prograde orbits: $L_z^i \geqslant 500$ kpc $\times$ km s^{-1}.

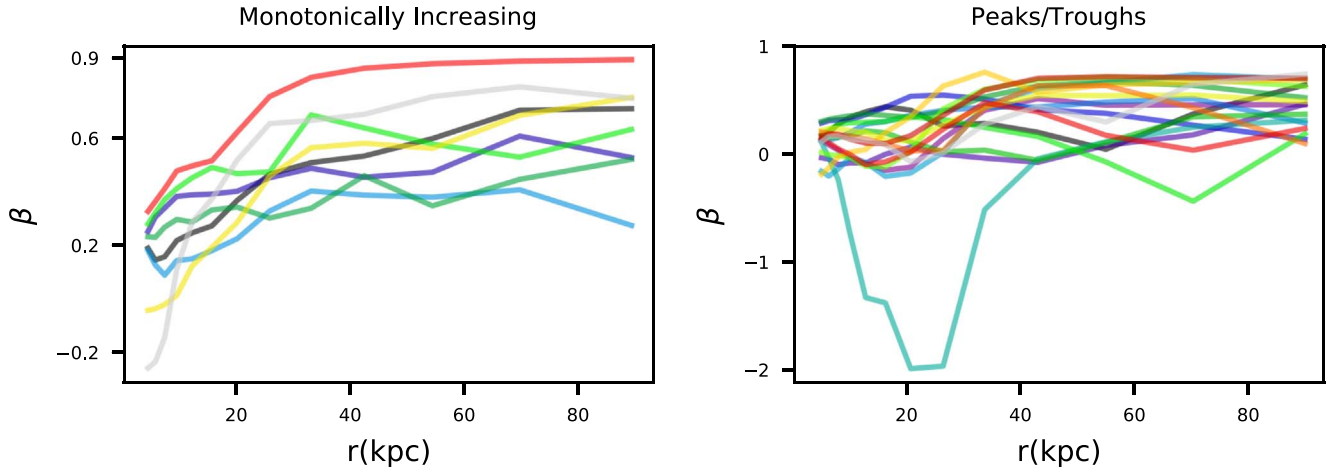

Figure 8. (Left panel) Profile of β with a monotonically increasing radial profile; 32% of the halos are in this category. Almost all of them are from category $\mathcal{A}$, with one exception belonging to class $\mathcal{B}$. (Right panel) β radial profile for cases with peaks and troughs. About 68% of the halos belong to this category, of which only 29% belong to category $\mathcal{A}$. This means that care must be taken in interpreting the observed peaks/troughs in the β radial profile, as it might be an indication of different selection criteria.

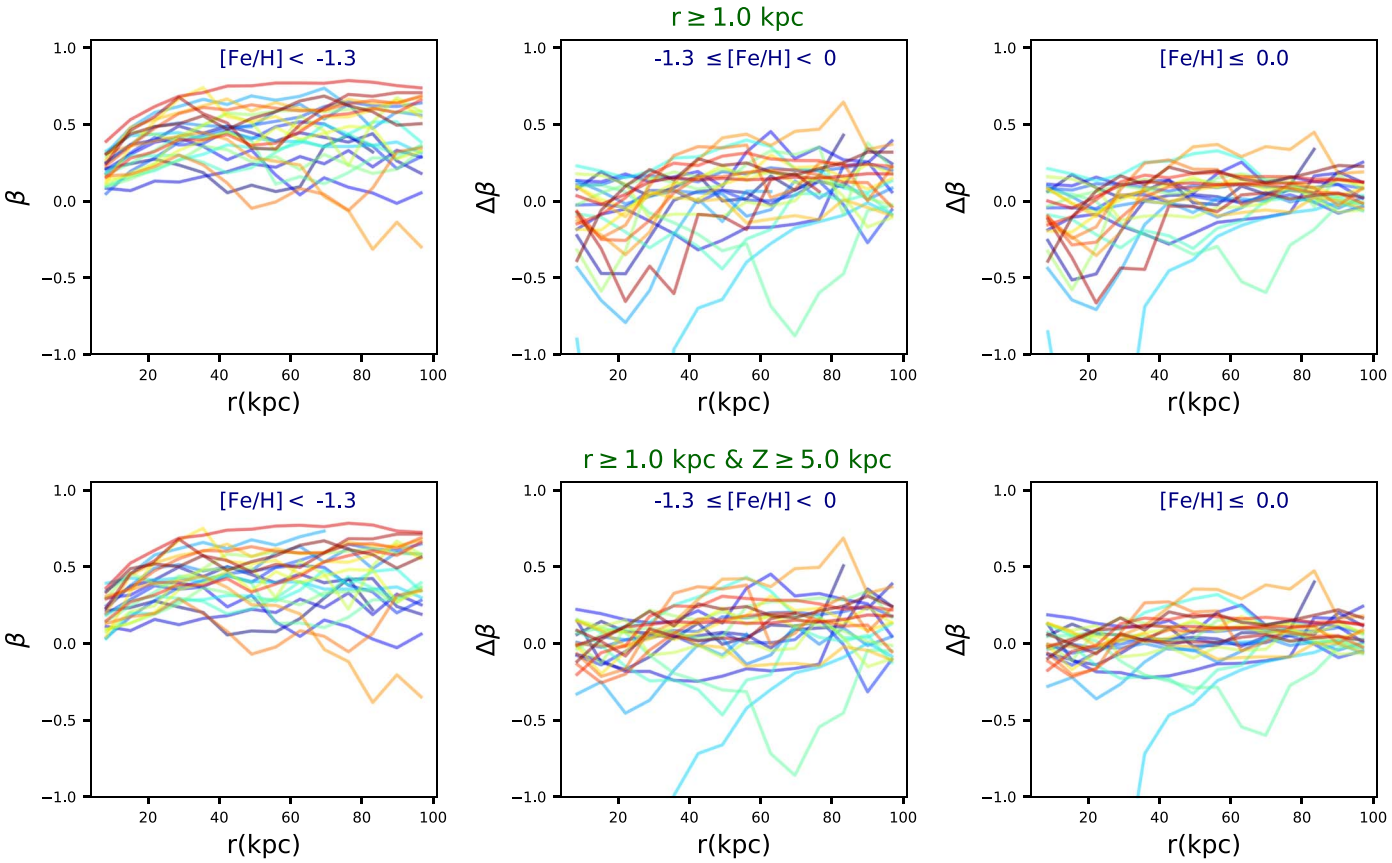

Figure 9. The β radial profile for stars located at $r \geqslant 1$ kpc (top panels) and with $r \geqslant 1$ kpc and $Z \geqslant 5$ kpc (bottom panels). In each row, from left to right, we consider stars with [Fe/H] $\leqslant -1.3$, $-1.3 \leqslant$ [Fe/H] $\leqslant 0$, and [Fe/H] $\leqslant 0.0$. While in the left panels, we present the β itself to facilitate the comparison, in the middle and right panels, we compute $\delta\beta$ subtracting the β from the left panel with [Fe/H] $\leqslant -1.3$. It is clearly seen that expanding over the range of metallicity, on average, diminishes the β.

While there are some variations on the exact behavior of individual galaxies, it is generally true that stars on radial orbits have a slightly higher β than the retrograde and prograde orbits. That is expected, as radial orbits have generally higher σ_r, and thus their β would be higher based on Equation (1). On the contrary, stars on retrograde and prograde orbits seem to have similar trends, though stars on prograde orbits have slightly higher β than the retrograde ones.

4.4. Impact of Eccentricity on the β Radial Profile

As the next case, here we analyze the impact of the orbital eccentricity on the β radial profile. The eccentricity is

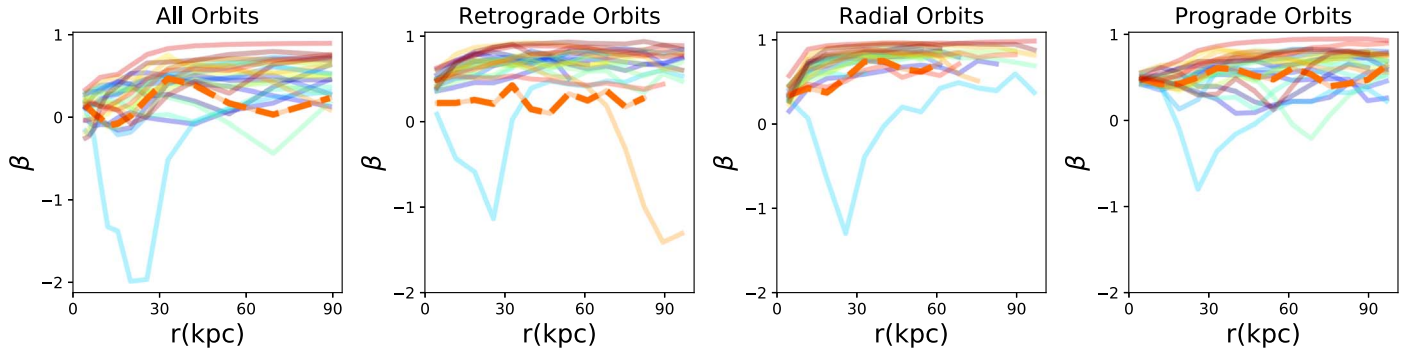

Figure 10. The β profile for stars of different orbital types. From left to right, we study the β radial profile for all, retrograde, radial, and prograde orbits. It is generally seen that stars on radial orbits have slightly higher β than the retrograde and prograde orbits. On the contrary, stars on retrograde and prograde orbits show similar trends in the β radial profile.

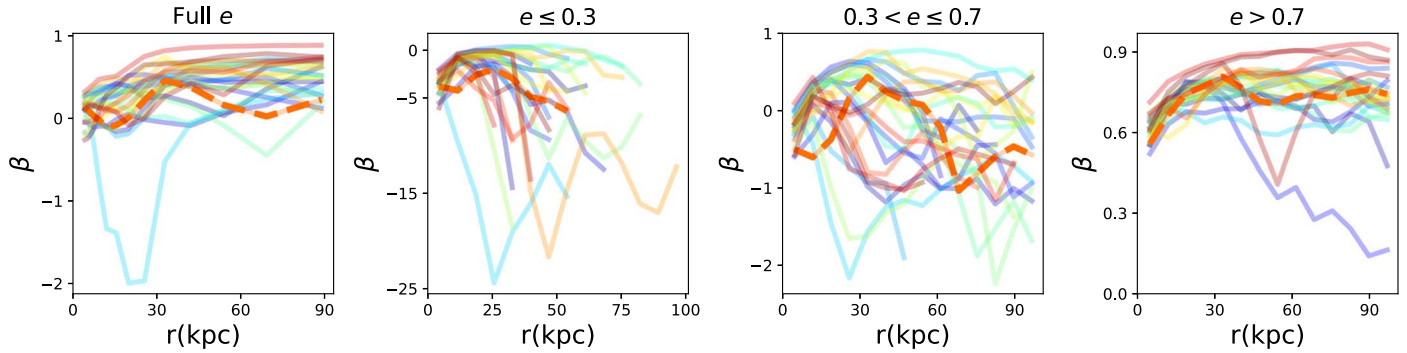

Figure 11. The β profile for different eccentric orbits. From left to right, we present the entire population of stars and stars with $e \leqslant 0.3$, $0.3 \leqslant e \leqslant 0.7$, and $e \geqslant 0.7$. It is noted that low-eccentricity stars have lower β than the parent population, as such stars are on nearly circular orbits. On the other hand, stars with higher eccentricities are more on radial orbits than tangential, producing higher β values.

approximately defined as

$$e \simeq \sqrt{1 - \left(\frac{L}{L_{\rm circ}}\right)^2}, \tag{4}$$

where $L_{\rm circ} \simeq \sqrt{GM(r_c)r_c}$, with $M(r_c)$ referring to the total mass interior to r_c describing the circular radii; see Equation (3) in Merritt (2015) and Emami et al. (2021b) for more details.

We note that Equation (4) is an approximate expression for the orbital eccentricity. This, together with the above estimation for $L_{\rm circ}$, gives rise to a negative result inside the square root in Equation (4) for a very small population of stars. As this is a consequence of a breakdown in the above assumption for that population of stars, we remove them from our sample. Finally, to check that Equation (4) eccentricity gives rise to a reasonable result for the eccentricity, we took a slightly different approach (see, for instance, Equations (1) and (2) of Mackereth et al. 2019). While the second scheme also fails for stars with a pericenter less than the softening length of the TNG simulation in which we do not have a well-defined expression for the gravitational potential, our results in the overlapping region indicate a satisfactory correspondence. Owing to this, in what follows, we use Equation (4) and infer the eccentricity accordingly.

Figure 11 presents $\beta(r)$ profiles for the entire stellar population (left panel) and three eccentricity-selected subsamples: $e \leqslant 0.3$, $0.3 \leqslant e \leqslant 0.7$, and $e \geqslant 0.7$. We note that low-eccentricity stars have a much lower β than the parent population. This is because these stars have nearly circular orbits, with σ_r being much lower than σ_θ and σ_ϕ. On the other hand, stars with higher eccentricities are more on radial orbits than tangential, producing higher β values.

Since the above eccentricity cut led to a substantial variation in the β radial profile, to explore its impact further, in Figure 12, we draw the 1D probability distribution function of eccentricity. From left to right, we analyze the distribution for the entire population of stars, those restricted to radii $1 \leqslant r/\mathrm{kpc} \leqslant 10$, and those in the range $10 \leqslant r/\mathrm{kpc} \leqslant 100$. From the plot, it is evident that in most cases, the eccentricity peaks between 0.2 and 0.4. Furthermore, there is a signal of bimodality in the eccentricity distribution. More explicitly, while in lower distances, the eccentricity is more concentrated on lower values, and at large radii, it shows some level of bimodality in which we have two peaks in the eccentricity distribution: one at relatively small radii and another at very high values.

Finally, Figure 13 presents the 2D distribution for the radial dependency of the eccentricity for a subsample of four galaxies from our galaxy sample. In each plot, we also show the Spearman correlation between the radius and the eccentricity. It is clearly seen that these two quantities are uncorrelated. Furthermore, different galaxies have their eccentricity peaks at different values and locations. For example, while galaxies 4 and 25 have a standard eccentricity peak of 0.2–0.5 in $r \leqslant 10$ kpc, galaxies 12 and 20 show some level of bimodality in the radial dependency of the eccentricity. It is seen that in these galaxies, there is a very high eccentric distribution at very low radii, followed by a second peak at $r \leqslant 10$ kpc. Perhaps such a bimodal distribution in the eccentricity is originated by galaxy mergers. However, this hypothesis must be validated, and we leave this to future work.

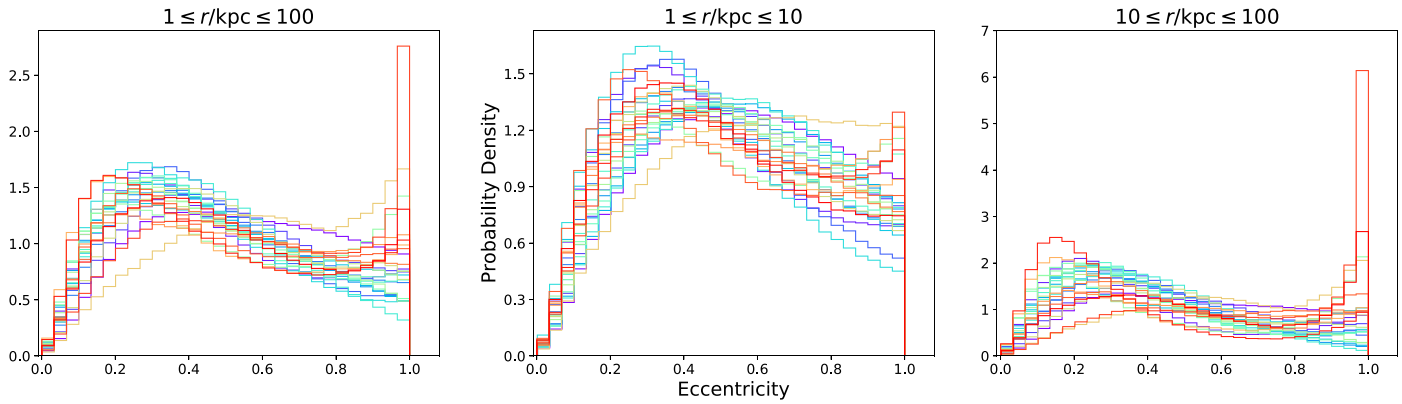

Figure 12. The 1D distribution of the eccentricity of stars in our galaxy sample. Quite interestingly, most galaxies have an eccentricity peak between 0.2 and 0.4. In very few cases, there is a second peak at higher eccentricities of about 1.0 coming from those stars located at larger distances.

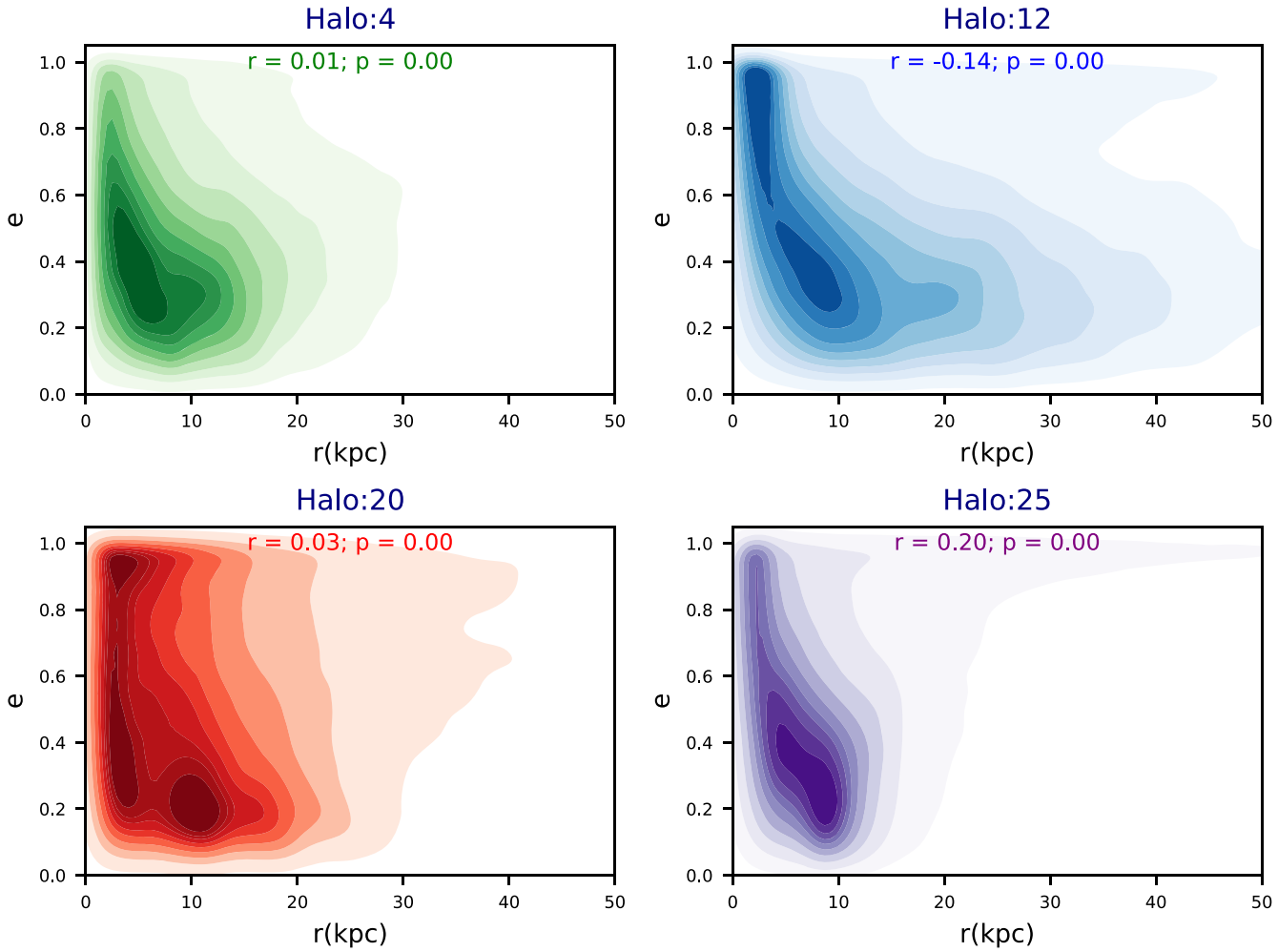

Figure 13. The 2D distribution plot of the radii vs. the eccentricity for a subsample of four galaxies from our galaxy sample. The Spearman correlation demonstrates that the eccentricity is uncorrelated with the radii.

4.5. The β Energy Profile

Since energy is an integral of motion, the β-energy profile, $\beta_{\rm E}$, may measure the velocity anisotropy in a less biased manner. It is then intriguing to compare the β radial (referred to as $\beta_{\rm r}$ in this section) and energy profiles against each other and check their similarities.

Figure 14 shows the $\beta_{\rm E}$ profile for different galaxies in our sample. To infer $\beta_{\rm E}$, the stellar energy is read directly from the TNG outputs. We then generate some energy bins, from the energy minimum to its maximum value, and compute $\beta_{\rm E}$ for each of these individually. As the energy range differs from one galaxy to another, the energy minimum and maximum are not the same for different galaxies. Furthermore, to ensure that in computing $\beta_{\rm E}$, we use stars similar to those used in computing $\beta_{\rm r}$, we imply a spatial cut of 1 kpc $\leqslant r \leqslant$ 100 kpc. Overlaid on each panel, we also present the $\beta_{\rm r}$ profile inferred for the

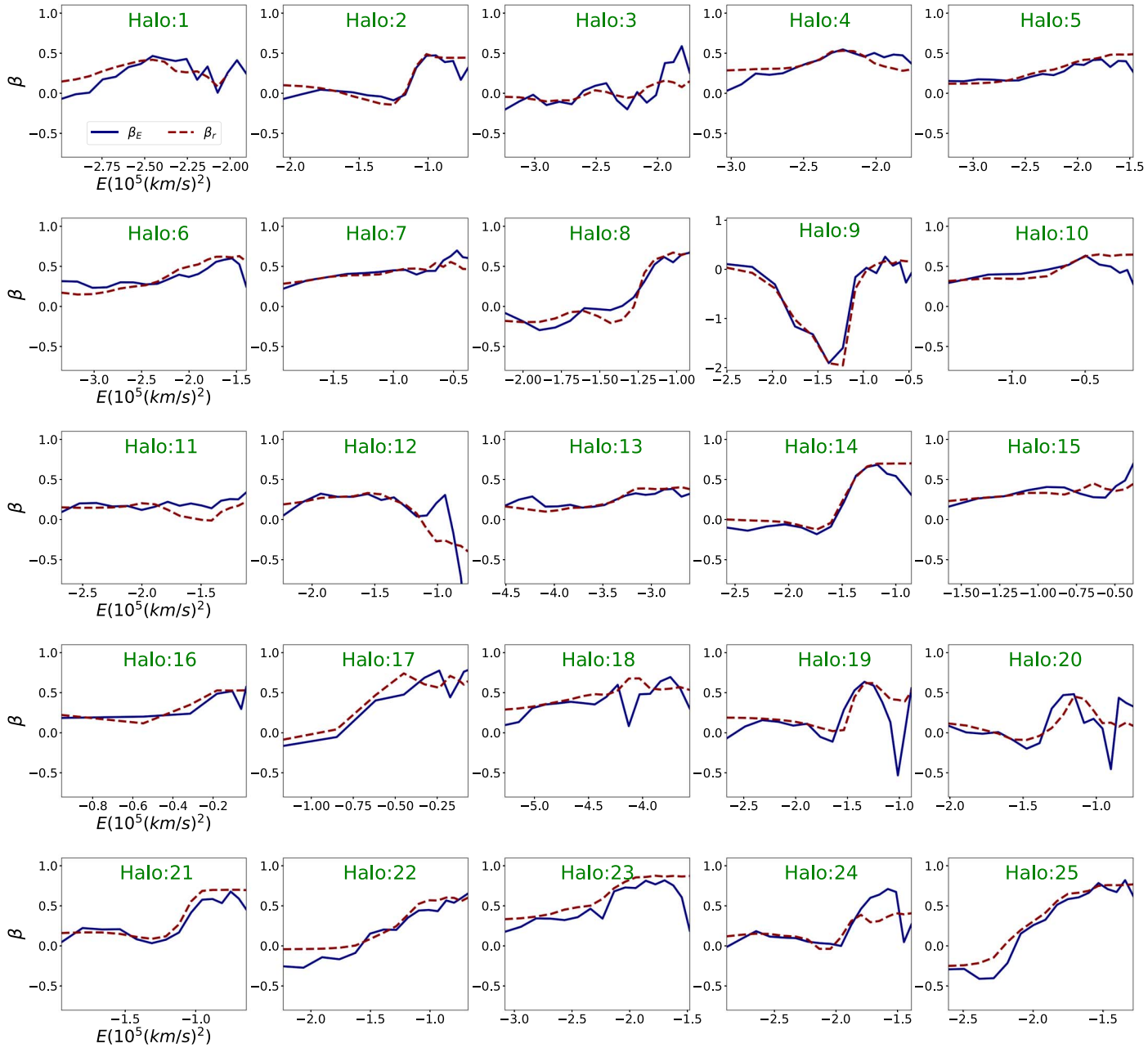

Figure 14. The β energy profile vs. the β radial profile for different halos in our galaxy sample. For each energy shell, we infer the median distance of stars and compute the β_r for that location. In inferring the β_E, we use a spatial cut of 1 kpc $\leqslant r \leqslant$ 100 kpc.

median distance in each energy shell. More explicitly, in every energy shell used in computing the β_E profile, we read off the median of the stellar distance to the center and compute the β_r at that particular position. In each panel, the solid blue line refers to β_E, while the dashed red line describes the β_r profile. The overall agreement between β_E and β_r is remarkable. There are, however, some differences between these profiles that are worth quantifying. For this purpose, we write an empirical estimator:

$$\delta\beta_{\mathcal{ER}} \equiv \frac{\sum_i |\beta_E^i - \beta_r^i|}{\sum_i |\beta_E^i|}. \quad (5)$$

Next, in a way similar to that in Section 4.1.1, we make distinct halo classes based on the magnitude of $\delta\beta_{\mathcal{ER}}$. We make three halo categories, as listed below.

1. *Category* $\mathcal{A}_\mathcal{E}$: $\delta\beta_{\mathcal{ER}} \leqslant 0.35$. The beta radial and energy profiles for halos that are part of this class are quite similar. There are 17 halos in this category, including halos [4, 5, 6, 7, 8, 9, 10, 13, 14, 15, 16, 17, 18, 21, 22, 23, 25]. Comparing the halos in this category with the ones in $\mathcal{A}$, it is seen that in 65% of the cases, the halo from class $\mathcal{A}$ is also part of class $\mathcal{A}_\mathcal{E}$.
2. *Category* $\mathcal{B}_\mathcal{E}$: $0.35 \leqslant \delta\beta_{\mathcal{ER}} \leqslant 0.70$. Halos in this class show a mild difference from the radial to the energy profile. There are six halos in this class, including halos [1, 2, 11, 12, 19, 24]. From this list, only one case is part of $\mathcal{B}$, and one is from $\mathcal{A}$, while the rest are part of class $\mathcal{C}$.
3. *Category* $\mathcal{C}_\mathcal{E}$: $\delta\beta_{\mathcal{ER}} \geqslant 0.70$. The β_E versus β_r in this class is not matched. There are two different halos that are part

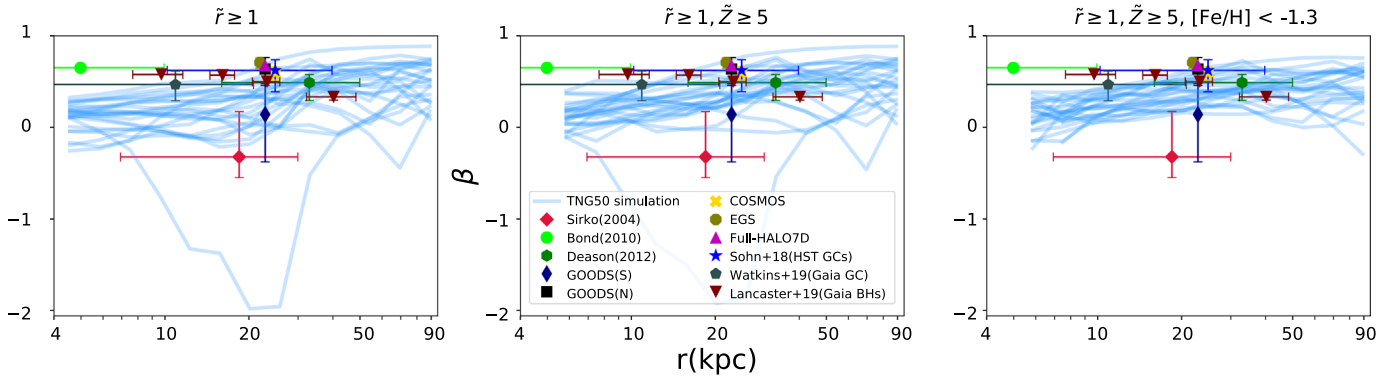

Figure 15. Comparison between the β radial profile inferred from the TNG50 simulation using different selection criteria and various isolated data points from different observations. From left to right, we present the β profile with $\tilde{r} \geqslant 1$, $\tilde{r} \geqslant 1$, $\tilde{Z} \geqslant 5$ and $\tilde{r} \geqslant 1$, $\tilde{Z} \geqslant 5$, [Fe/H] $\leqslant -1.3$. In each panel, we also present the data points from Sirko et al. 2004, Bond et al. 2010, Deason et al. 2012, Sohn et al. 2018, Watkins et al. 2019, Lancaster et al. 2019, and Cunningham et al. 2019. It is seen that adding the metallicity cut with [Fe/H] $\leqslant -1.3$ somewhat reduces the diversity of models, as it substantially removes the young stars. On the contrary, the model diversity is maximal for $\tilde{r} \geqslant 1$, in which the diversity is comparable to the error bars from changing the observations. This demonstrates that including/altering the stellar types may significantly affect the β, causing different observations to have different results.

of this category, including [3, 20], and both of these halos are part of $\mathcal{C}$.

5. Connection to Observations

Having presented the β radial profile using different cuts, here we make an in-depth comparison between the above theoretical outcomes and the actual observational results. There are two different aspects that could be addressed in our comparison: first, the overall amplitude of the velocity anisotropy β, and second, its radial shape. While the first case is easier to study, the second is more challenging, as it may depend on different selections/cuts employed for stars that are then less natural. Owing to this, we make the comparison for different selections, including $\tilde{r} \geqslant 1$, $\tilde{r} \geqslant 1$, $\tilde{Z} \geqslant 5$ and $\tilde{r} \geqslant 1$, $\tilde{Z} \geqslant 5$, [Fe/H] $\leqslant -1.3$.

Below, we first point out a few different observational studies. We then make a comparison between our results and different observations.

5.1. Observational Constraints on $\beta(r)$

Observations measuring β employ various approaches using different tracers, including K giants, the BHB, RR Lyrae, and subdwarf stars in the solar neighborhood. Below, we review a few different observational studies.

Sirko et al. (2004) used a sample of BHB stars from the SDSS survey and inferred the radial and tangential velocity dispersions in the radial distance $5 \leqslant r/\mathrm{kpc} \leqslant 30$. In Figure 15, we have converted these values to some estimators for β in the aforementioned interval.

Bond et al. (2010) used a large sample (18.8 million) of main-sequence stars derived from SDSS and POSS astrometry and estimated $\beta \simeq 0.65$ in a radial range $3 \leqslant r/\mathrm{kpc} \leqslant 13$.

Deason et al. (2012) used distant BHB stars with galactocentric distances in the radial range $16 < r/\mathrm{kpc} < 48$ as the kinematic tracers of the MW dark halo and inferred $\beta \approx 0.5$, in line with local solar neighborhood studies.

Sohn et al. (2018) used their HST proper-motion measurements from 16 globular clusters (GCs) and found $\beta = 0.609^{0.13}_{-0.229}$ in the galactic distance range from 10 to 40 kpc.

Watkins et al. (2019) used a sample of 34 halo GCs from Gaia data spanning the radial range 2–21.1 kpc and estimated the velocity anisotropy $\beta = 0.46.^{+0.15}_{-0.19}$.

Lancaster et al. (2019) assembled a very high purity set of 3064 BHBs using the spectroscopic data from SDSS, as well as the astrometric data from the Gaia satellite. They computed β (see the orange line in their Figure 9) in the galactic center radius range 7–50 kpc. Their extended data points allow us to probe the radial evolution of β. However, since it only covers four data points, we present the results in our generic comparison in Figure 15.

Cunningham et al. (2019) used the data from Halo Assembly in Lambda Cold Dark Matter: observation in 7 Dimensions (HALO7D), consisting of the Keck II/DEIMOS spectroscopic and HST data applied for the main-sequence turnoff stars, and estimated the β for the full HALO7D sample, as well as its individual fields, including COSMOS, GOODS-N, GOODS-S, and EGS. The details of the data points and β values are given in Table 3 of Cunningham et al. (2019). In Figure 15, we present all of the results for the full sample, as well as individual ones.

Kafle et al. (2012) used a sample of 4664 BHB stars chosen from SDSS/SEGUE and measured β out to 25 kpc while estimating it up to 60 kpc. There are various trends seen in the data, including a smooth value of $\beta \sim 0.5$ in the inner part of the halo ($9 \leqslant r/\mathrm{kpc} \leqslant 12$), followed by a rather sharp falloff of β in the range $r \sim 13$–18 kpc, a minimum of $\beta = -1.2$ at $r = 17$ kpc, and an extra rising of β at larger radii. At the outer parts of the halo, in the interval $25 \leqslant r/\mathrm{kpc} \leqslant 56$, the actual measurement of β is not possible owing to the lack of proper motions. They predicted $\beta \sim 0.5$ in this interval. In Figure 16 (top panels), we focus on these data and compare them with the TNG50 results obtained using different cuts.

King et al. (2015) used a sample of 6174 faint F-type stars from the Hectospec spectrograph on the MMT telescope plus a sample of 3330 BHB stars from SDSS and estimated β within 6–30 kpc of the MW. The results are presented in Table 3 of King et al. (2015). In the middle panels of Figure 16, we present their data and compare them against the simulation results obtained using different cuts.

Bird et al. (2019) made a sample of 7664 metal-poor K giants using the LAMOST catalog and measured β at galactocentric radii between 5 and 100 kpc. As they matched

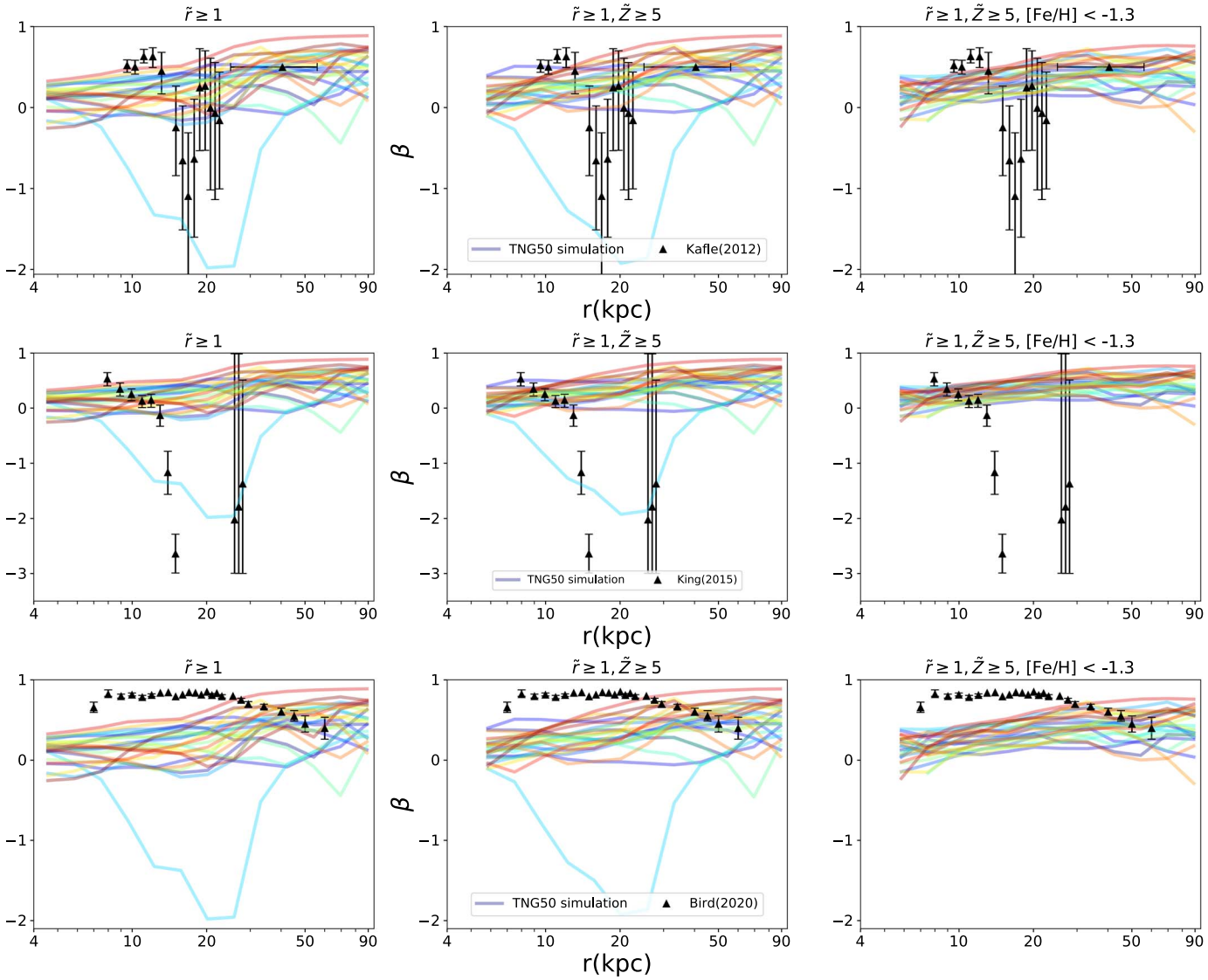

Figure 16. Comparison of the β radial profile from the TNG50 simulation with three extended observational data points. The top panels present the data from Kafle et al. (2012), the middle panels show the results from King et al. (2015), and the bottom panels present the results from Bird et al. (2019). In each row, we present the TNG50 results using different selection criteria. It is seen that there is a good overall agreement between the TNG50 results and these extended observations. The model diversity is somewhat comparable to the error bars in Kafle et al. (2012), while it is smaller than the ones from King et al. (2015). Finally, while the first two panels show a prominent dip in the β radial profile, the third one does not show any particular dips. Since proper motion has not been considered in the first two cases, the third one may be more reliable.

their LOS velocities to the proper motions from the Gaia data, their final results might be less bias compared with earlier literature, such as Kafle et al. (2012) and King et al. (2015). In the bottom panels of Figure 16, we present their results, comparing them against the TNG50 results obtained using different cuts.

5.2. Comparison between Theory and Observation

Here we make a comparison between the aforementioned observational results listed in Section 5.1 and the outcome of the TNG50 simulation obtained from employing different selection criteria.

Before we dig into the details of the comparison, we make some remarks regarding the potential impact of substructures on the β radial profile. Observationally, Bird et al. (2019) showed that including the effect of the Sagittarius stream may lead to a dip in the β radial profile. Consequently, the inclusion and removal of the substructures are, in principle, very important. Theoretically, there have been some studies (see, e.g., Loebman et al. 2018, and references therein) showing that the substructures may alter the shape of the β radial profile. In the context of the TNG50 simulations specifically, the substructures are all removed from the central halos and are only part of the group catalog. As the entire focus of this paper is on the central halos, our analysis is safe from the direct impact of the substructures. Our analysis is, however, missing the indirect impact of substructures through their gravitational potential. This is much harder to quantify, as we need to model their orbits, which require a greater time cadence in the outputs. We therefore ignore this effect in the current work and leave its analysis to a future study.

We split the comparison into two different sets, presenting them in two separate plots.

In Figure 15, we present the individual data points from seven different observational data sets (Sirko et al. 2004; Bond et al. 2010; Deason et al. 2012; Sohn et al. 2018; Watkins et al. 2019; Lancaster et al. 2019; Cunningham et al. 2019). We add the TNG50 results obtained from three different selection criteria: $\tilde{r} \geqslant 1$ (left panel), $\tilde{r} \geqslant 1$, $\tilde{Z} \geqslant 5$ (middle panel), and $\tilde{r} \geqslant 1$, $\tilde{Z} \geqslant 5$, [Fe/H] $\leqslant -1.3$ (right panel). From the plot, it is inferred that the model diversity is maximal for the left panel, while it is minimal in the right panel with metallicity cuts. This means that it is easier to find a theoretical model that matches more observations from the left panel than the right. Furthermore, despite the fact that there is no single galaxy that matches all of the different observational points, there are quite a few of them that get close to quite a few observations, especially for the left and middle panels with no metallicity cuts. To summarize, the diversity of different realizations from the TNG50 is comparable to the differences between various observations. This means that TNG50 models can explain different observations.

In Figure 16, we focus on three extended observations from Kafle et al. (2012), King et al. (2015), and Bird et al. (2019) in which we put the data from three individual observations in different rows and make the comparison against the TNG50 results. Again, different panels refer to various selection criteria. The advantage of using the same observation is that we are generally less biased by different selection criteria from various observations. However, we are still affected by some systematic errors owing to the fact that the observational data of Kafle et al. (2012) and King et al. (2015) were collected before Gaia. This is likely to introduce some biases owing to the lack of the actual treatment of the proper motion (see, e.g., Hattori et al. 2017, for more details). Consequently, the interpretation of the β radial profile might not be straightforward. As is seen from the bottom row, the analysis of Bird et al. (2019) did not lead to a strong dip in the β radial profile.

From the plot, it is seen that there are few models that get very close to some data points and within their error bars. Again, the model capabilities in reproducing the data slightly depend on different selection criteria.

In summary, the TNG50 results are in overall good agreement with different observational points, though some of these are closer to the data.

Since the diversity of TNG50 models diminishes by considering a metallicity cut, we expect to have more models near the peak of agreement and less away from the peak. On the contrary, for models with a higher diversity, the chances of finding a model realization that passes close to the rare data points are higher, though the population of models near the peak of agreement is less.

6. Conclusions

In this paper, we analyzed the stellar kinematics as traced with the velocity anisotropy, β, profile for a sample of 25 MW-like galaxies from the TNG50 simulation. We made an in-depth study of the β radial and energy profiles at a redshift of $z = 0$, exploring the impact of different selection criteria on the aforementioned quantities.

Below, we summarize the main takeaways from this study.

1. It is observed that the stellar metallicity is negatively correlated with the stellar age, with a Spearman coefficient $|r| \simeq 0.5$–0.8. Furthermore, it is also negatively correlated with the locations of stars, meaning that older stellar populations are mostly located in the galaxy outskirts, while younger ones are closer to the center. This is expected, as the MW is still in its star-forming stage. Based on this, we explored the impact of different metallicity cuts on the velocity anisotropy of stars.
2. We inferred the β radial profile using different selection criteria and made halo classifications, categories $\mathcal{A}$–$\mathcal{C}$, based on the sensitivity of their profiles on various cuts.
3. Halos that are part of $\mathcal{A}$ class show a very mild sensitivity to different selections, where $\delta\beta \leqslant 0.35$. Members of category $\mathcal{B}$ exhibit some level of sensitivity, with $0.35 \leqslant \delta\beta \leqslant 0.7$, to different cuts. Finally, halos associated with $\mathcal{C}$ show very strong dependencies, $\delta\beta \geqslant 0.7$, to model selections. We showed that 48%, 16%, and 36% of the halos are in each of these classes, respectively.
4. We analyzed the β radial profile and demonstrated that it is divided into either monotonically increasing profiles (32% of the halos) or the ones with peaks/troughs (68% of the population). It is shown that the β profile from the monotonically increasing class smoothly increases from the interior to the exterior part of the halo, while β associated with the class with peaks/troughs experiences some local fluctuations. We further demonstrate that almost all of the halos from the first class are part of category $\mathcal{A}$, with only one exception being part of class $\mathcal{B}$. On the contrary, members of the class with peaks/troughs are mostly part of categories $\mathcal{B}$ or $\mathcal{C}$, with only 29% of them being part of category $\mathcal{A}$. This means that care should be taken in interpreting the observed peaks/troughs, as they might depend on the actual selection criteria.
5. We probed the impact of different metallicity cuts on the β profile and demonstrated that older stars are less rotationally supported and thus have higher β. On the other hand, younger stars are more rotationally supported and have lower β.
6. We explored the impact of different eccentricity-based radial cuts on the β radial profile. More explicitly, we divided stars into low-, medium-, and high-eccentricity chunks. This explicitly showed that low-eccentricity orbits correspond to lower β than high-eccentricity orbits. This is expected, as low-eccentricity orbits correspond to less radial velocity variance, which naturally leads to smaller β.
7. We computed β for different stellar types, demonstrating that stars on radial orbits have a higher velocity anisotropy than those on prograde and retrograde orbits. This is also expected, as radial orbits have a lower absolute angular momentum and thus higher radial velocity variance.
8. Moving to the energy space, we calculated the β energy profile and compared that with the β radial profile, where we made another halo classification based on their similarities/differences. We explicitly showed that 65% of the halos that present very mild sensitivity on different selection criteria in the real space are among those for which the β radial and energy profiles are very closely related. On the contrary, halos for which the β radial/energy profiles are rather different are entirely part of category $\mathcal{C}$. This again establishes that we should be very

careful when drawing any conclusions from the β analysis.

9. Furthermore, we proposed that one quantitative way to examine whether the observational results are somewhat robust is to also compute the β energy profile and compare that with the β radial profile. Based on our conclusion, it is likely that those with very similar profiles are more robust against altering the selection criteria than the ones with different profiles. However, as already indicated above, the current analysis and comparison are purely theoretical. From the observational perspective, we need to estimate the gravitational potential. This paper is not meant to show that we identify the unbiased sample of stars using this comparison, merely that for a chosen stellar sample, this comparison may indicate how much the chosen sample might be sensitive to different criteria.
10. Ultimately, we overlaid our theoretical outcomes, with a few different selection criteria, on top of some recent observational results and compared them with each other. Our comparison was made at the level of isolated data points, in which each observation gives us only one point, as well as extended observations, in which the β radial profile is reported in more than a single point for a particular observation. The latter one is more meaningful, since we are not affected by the biases coming from changing the observations or selection criteria. It is shown that there are reasonable agreements between the theoretical predictions and the observational results for both the isolated data points and the extended observations. It is seen for most of the halos that there are some data points that easily pass through the profile.

It is a great pleasure to thank Sirio Belli, Sownak Bose, Shep Doeleman, and Sandro Tacchella for very insightful conversations. R.E. acknowledges support by the Institute for Theory and Computation at the Center for Astrophysics. We thank the supercomputer facility at Harvard, where most of the simulation work was done. M.V. acknowledges support through an MIT RSC award, a Kavli Research Investment Fund, NASA ATP grant NNX17AG29G, and NSF grants AST-1814053, AST-1814259, and AST-1909831. F.M. acknowledges support through the Program "Rita Levi Montalcini" of the Italian MIUR. The TNG50 simulation was realized with computing time granted by the Gauss Center for Supercomputing (GCS) under GCS Large-Scale Projects GCS-DWAR on the GCS share of the supercomputer Hazel Hen at the High Performance Computing Center Stuttgart (HLRS).

Software: matplotlib (Hunter 2007), numpy (van der Walt et al. 2011), scipy (Oliphant 2007), seaborn (Waskom et al. 2020), pandas (Reback et al. 2021), h5py (de Buyl et al. 2016).

Data Availability

Data directly related to this manuscript and its figures are available to share on reasonable request from the corresponding author. The IllustrisTNG and TNG50 simulations are publicly available and accessible at www.tng-project.org/data (Nelson et al. 2019b).

ORCID iDs

Razieh Emami https://orcid.org/0000-0002-2791-5011
Lars Hernquist https://orcid.org/0000-0001-6950-1629
Mark Vogelsberger https://orcid.org/0000-0001-8593-7692
Xuejian Shen https://orcid.org/0000-0002-6196-823X
Joshua S. Speagle (沈佳士) https://orcid.org/0000-0003-2573-9832
Jorge Moreno https://orcid.org/0000-0002-3430-3232
Charles Alcock https://orcid.org/0000-0002-7892-3636
Shy Genel https://orcid.org/0000-0002-3185-1540
John C. Forbes https://orcid.org/0000-0002-1975-4449
Federico Marinacci https://orcid.org/0000-0003-3816-7028
Paul Torrey https://orcid.org/0000-0002-5653-0786

References

Abadi, M. G., Navarro, J. F., & Steinmetz, M. 2006, MNRAS, 365, 747
Adams, J. J., Gebhardt, K., Blanc, G. A., et al. 2012, ApJ, 745, 92
Adams, J. J., Simon, J. D., Fabricius, M. H., et al. 2014, ApJ, 789, 63
Anders, F., Chiappini, C., Minchev, I., et al. 2017, A&A, 600, A70
Battaglia, G., Helmi, A., Tolstoy, E., et al. 2008, ApJL, 681, L13
Beers, T. C., Carollo, D., Ivezić, Ž, et al. 2012, ApJ, 746, 34
Binney, J. 1980, MNRAS, 190, 873
Bird, J. C., Loebman, S. R., Weinberg, D. H., et al. 2021, MNRAS, 503, 1815
Bird, S. A., Xue, X.-X., Liu, C., et al. 2019, AJ, 157, 104
Bird, S. A., Xue, X.-X., Liu, C., et al. 2021, ApJ, 919, 66
Bond, N. A., Ivezić, Ž, Sesar, B., et al. 2010, ApJ, 716, 1
Chiba, M., & Yoshii, Y. 1998, AJ, 115, 168
Cinzano, P., & van der Marel, R. P. 1994, MNRAS, 270, 325
Courteau, S., Cappellari, M., de Jong, R. S., et al. 2014, RvMP, 86, 47
Cunningham, E. C., Deason, A. J., Guhathakurta, P., et al. 2016, ApJ, 820, 18
Cunningham, E. C., Deason, A. J., Sanderson, R. E., et al. 2019, ApJ, 879, 120
de Buyl, P., Huang, M.-J., & Deprez, L. 2016, arXiv:1608.04904
Deason, A. J., Belokurov, V., Evans, N. W., & An, J. 2012, MNRAS, 424, L44
Dejonghe, H., & Merritt, D. 1992, ApJ, 391, 531
Dekel, A., Stoehr, F., Mamon, G. A., et al. 2005, Natur, 437, 707
Diakogiannis, F. I., Lewis, G. F., & Ibata, R. A. 2014a, MNRAS, 443, 598
Diakogiannis, F. I., Lewis, G. F., & Ibata, R. A. 2014b, MNRAS, 443, 610
Diemand, J., Madau, P., & Moore, B. 2005, MNRAS, 364, 367
Dietz, S. E., Yoon, J., Beers, T. C., & Placco, V. M. 2020, ApJ, 894, 34
El-Badry, K., Wetzel, A. R., Geha, M., et al. 2017, ApJ, 835, 193
Emami, R., Hernquist, L., Alcock, C., et al. 2021a, ApJ, 918, 7
Emami, R., Genel, S., Hernquist, L., et al. 2021b, ApJ, 913, 36
Emami, R., Hernquist, L., Alcock, C., et al. 2021c, AAS Meeting, 53, 324.07
Frankel, N., Sanders, J., Rix, H.-W., Ting, Y.-S., & Ness, M. 2019, ApJ, 884, 99
Gaia Collaboration, Helmi, A., van Leeuwen, F., et al. 2018, A&A, 616, A12
Gallazzi, A., Charlot, S., Brinchmann, J., White, S. D. M., & Tremonti, C. A. 2005, MNRAS, 362, 41
Gilmore, G., Wilkinson, M. I., Wyse, R. F. G., et al. 2007, ApJ, 663, 948
Grand, R. J. J., Helly, J., Fattahi, A., et al. 2018, MNRAS, 481, 1726
Hani, M. H., Ellison, S. L., Sparre, M., et al. 2019, MNRAS, 488, 135
Hattori, K., Valluri, M., Loebman, S. R., & Bell, E. F. 2017, ApJ, 841, 91
Hattori, K., Yoshii, Y., Beers, T. C., Carollo, D., & Lee, Y. S. 2013, ApJL, 763, L17
Huang, Y., Liu, X.-W., Zhang, H.-W., et al. 2015, RAA, 15, 1240
Hunter, J. D. 2007, CSE, 9, 90
Jeans, J. H. 1915, MNRAS, 76, 70
Johnson, J. W., Weinberg, D. H., Vincenzo, F., et al. 2021, MNRAS, 508, 4484
Kafle, P. R., Sharma, S., Lewis, G. F., & Bland-Hawthorn, J. 2012, ApJ, 761, 98
Kewley, L. J., & Ellison, S. L. 2008, ApJ, 681, 1183
King, C. I., Brown, W. R., Geller, M. J., & Kenyon, S. J. 2015, ApJ, 813, 89
Kleyna, J. T., Wilkinson, M. I., Evans, N. W., & Gilmore, G. 2001, ApJL, 563, L115
Koch, A., Kleyna, J. T., Wilkinson, M. I., et al. 2007, AJ, 134, 566
Krajnović, D., Cappellari, M., Emsellem, E., McDermid, R. M., & de Zeeuw, P. T. 2005, MNRAS, 357, 1113
Lancaster, L., Koposov, S. E., Belokurov, V., Evans, N. W., & Deason, A. J. 2019, MNRAS, 486, 378
Loebman, S. R., Valluri, M., Hattori, K., et al. 2018, ApJ, 853, 196
Łokas, E. L. 2009, MNRAS, 394, L102
Łokas, E. L., Mamon, G. A., & Prada, F. 2005, MNRAS, 363, 918
Mackereth, J. T., Schiavon, R. P., Pfeffer, J., et al. 2019, MNRAS, 482, 3426
Mamon, G. A., Biviano, A., & Boué, G. 2013, MNRAS, 429, 3079
Mamon, G. A., & Łokas, E. L. 2005, MNRAS, 363, 705

Mashchenko, S. 2015, arXiv:1504.08273
Merritt, D. 1985, AJ, 90, 1027
Merritt, D. 2015, ApJ, 814, 57
Monachesi, A., Gómez, F. A., Grand, R. J. J., et al. 2016, MNRAS, 459, L46
Monachesi, A., Gómez, F. A., Grand, R. J. J., et al. 2019, MNRAS, 485, 2589
Morrison, H. L., Flynn, C., & Freeman, K. C. 1990, AJ, 100, 1191
Naidu, R. P., Conroy, C., Bonaca, A., et al. 2020, ApJ, 901, 48
Nelson, D., Pillepich, A., Springel, V., et al. 2019a, MNRAS, 490, 3234
Nelson, D., Springel, V., Pillepich, A., et al. 2019b, ComAC, 6, 2
Oliphant, T. E. 2007, CSE, 9, 10
Pillepich, A., Nelson, D., Springel, V., et al. 2019, MNRAS, 490, 3196
Rashkov, V., Pillepich, A., Deason, A. J., et al. 2013, ApJL, 773, L32
Reback, J., jbrockmendel, McKinney, W., et al. 2021, pandas-dev/pandas: Pandas 1.3.2, v1.3.2, Zenodo, doi:10.5281/zenodo.5203279
Sales, L. V., Navarro, J. F., Abadi, M. G., & Steinmetz, M. 2007, MNRAS, 379, 1464
Santucci, G., Brough, S., Scott, N., et al. 2020, ApJ, 896, 75
Schuster, W. J., Moreno, E., Nissen, P. E., & Pichardo, B. 2012, A&A, 538, A21
Sirko, E., Goodman, J., Knapp, G. R., et al. 2004, AJ, 127, 914
Smith, M. C., Evans, N. W., Belokurov, V., et al. 2009, MNRAS, 399, 1223
Sohn, S. T., Anderson, J., & van der Marel, R. P. 2012, ApJ, 753, 7
Sohn, S. T., Watkins, L. L., Fardal, M. A., et al. 2018, ApJ, 862, 52
Sommer-Larsen, J., Flynn, C., & Christensen, P. R. 1994, MNRAS, 271, 94
Stinson, G. S., Brook, C., Macciò, A. V., et al. 2013, MNRAS, 428, 129
Strigari, L. E., Bullock, J. S., Kaplinghat, M., et al. 2007, ApJ, 669, 676
Thom, C., Flynn, C., Bessell, M. S., et al. 2005, MNRAS, 360, 354
Tully, R. B., & Fisher, J. R. 1977, A&A, 500, 105
van der Walt, S., Colbert, S. C., & Varoquaux, G. 2011, CSE, 13, 22
Walker, M. G., Mateo, M., Olszewski, E. W., et al. 2007, ApJL, 667, L53
Walker, M. G., Mateo, M., Olszewski, E. W., et al. 2009, ApJ, 704, 1274
Waskom, M., Botvinnik, O., Ostblom, J., et al. 2020, mwaskom/seaborn: v0.10.0 (January 2020), v0.10.0, Zenodo, doi:10.5281/zenodo.3629446
Watkins, L. L., van der Marel, R. P., Sohn, S. T., & Evans, N. W. 2019, ApJ, 873, 118
Wilkinson, M. I., Kleyna, J. T., Evans, N. W., et al. 2004, ApJL, 611, L21
Wolf, J., Martinez, G. D., Bullock, J. S., et al. 2010, MNRAS, 406, 1220
Zuo, W., Du, C., Jing, Y., et al. 2017, ApJ, 841, 59